An actin-based viscoplastic lock ensures progressive body-axis elongation

Alicia Lardennois, Teresa Ferraro, Flora Llense, Michel Labouesse, Gabriella Pásti, Julien Pontabry, David Rodriguez, Samantha Kim, Christelle Gally, Pierre Mahou, et al.

An actin-based viscoplastic lock ensures progressive body axis elongation

Alicia Lardennois, Teresa Ferraro, Flora Llense & Michel Labouesse

CNRS UMR7622, Institut de Biologie Paris–Seine (IBPS), Sorbonne Université, Paris, France

Gabriella Pásti, Julien Pontabry, David Rodriguez, Samantha Kim, Christelle Gally & Michel Labouesse

IGBMC –CNRS UMR 7104, INSERM U964, Development and Stem Cells Department, Université de Strasbourg, Illkirch, France

Pierre Mahou & Emmanuel Beaurepaire

INSERM U1182 – CNRS/ UMR7645, Laboratoire d'Optique et Biosciences, Ecole Polytechnique, Paris, France

Julien Pontabry

RS2D, Mundolsheim, France

Shoichiro Ono

Departments of Pathology and Cell Biology, Winship Cancer Institute, Emory University School of Medicine, Atlanta, GA, USA

Corresponding author: michel.labouesse@upmc.fr

Abstract

A key step in animal development is the process of body axis elongation, laying out the final form of the entire animal. This critically depends on polarized cell shape changes[1], which rely on the interplay between intrinsic forces generated by molecular motors[2-5], extrinsic forces due to adjacent cells pulling or pushing on the tissue[6-9], and mechanical resistance forces due to cell and tissue elasticity or friction[10-12]. Understanding how mechanical forces influence morphogenesis at the cellular and molecular level remains a critical challenge[2]. Recent work outlined that cell shape changes occur through small incremental steps[2,4,5,13], suggesting the existence of specific mechanisms to stabilize cell shapes and counteract cell elasticity. Here, we identify a spectrin-kinase-formin network required to stabilize embryo shape when repeated muscle contractions promote *C. elegans* embryo axis elongation. Its absence induces complete axis retraction due to damage of epidermal actin stress fibers. Modeling predicts that a mechanical viscoplastic deformation process can account for embryo shape stabilization. Molecular analysis suggests that the physical basis for viscoplasticity originates from the progressive shortening of epidermal microfilaments induced by muscle contractions and FHOD-1 formin activity. Our work thus identifies an essential molecular lock acting in a developmental ratchet-like process.

C. elegans provides a simple and integrated model to study the cellular impact of mechanical forces. Its embryonic elongation only relies on cell shape changes and includes two phases depending on tension and stiffness anisotropies in the epidermis[12], and beyond the 2-fold stage on muscle activity[8] (Fig. 1a; Supplementary material). Importantly, neither stage relies on pulsatile actomyosin flows[12], as observed in the early *C. elegans* zygote, or during *Drosophila* gastrulation and germband extension[2,4,5,13]. Because muscles are tightly mechanically coupled to the epidermis through epidermal hemidesmosomes[14], their contractions also displace the epidermis. This can be monitored by tracking the anterior-posterior displacement of muscle nuclei and the circumferentially oriented epidermal actin filaments (Fig. 1b-b'''). Importantly, all muscles do not contract simultaneously (X. Yang and M. Labouesse, unpublished). Hence, when some areas of the epidermis are longitudinally compressed (red line in Fig. 1c'), others are stretched (green line in Fig. 1c') before eventually relaxing (Fig. 1c-c"; Fig. S1). Importantly, we previously established that the tension generated by muscle activity triggers a mechanotransduction pathway in the epidermis, which promotes axis elongation[8].

The relaxation observed after each muscle contraction raises a conundrum: how can muscle activity power embryonic elongation from 100 µm to 200 µm within an hour if cell elasticity brings cells back to their initial length after each contraction (Fig. 1d). One simple hypothesis would be that some mechanism stabilizes the transient body deformations induced by muscle activity (Fig. 1d'), as was proposed for *Drosophila* gastrulation or germband extension in processes involving myosin II[5,15,16]. To uncover this mechanism, we focused on the kinase PAK-1, which lies at the crossroads of

hemidesmosome remodelling[9] and actomyosin force regulation[17,18]. We first performed a feeding RNAi screen in a strong yet viable *pak-1* mutant, looking for enhancers of embryonic lethality and/or body morphology defects (Fig. 2a). This screen identified the gene *spc-1* encoding α-spectrin as a strong *pak-1* genetic enhancer leading to short hatchlings (58 µm on average), which were significantly shorter than *pak-1(tm403)* (178 µm) or *spc-1(RNAi)* (91 µm) hatchlings (Fig. 2b, Table S1). The study of this genetic interaction was further motivated by the identification of the central Src Homology 3 domain (SH3) of SPC-1 as an interactor of the N-terminal domain of PAK-1 in a yeast two-hybrid screen (Fig. 2c, Table S2). Both screens thus point to an interaction between SPC-1 and PAK-1.

To understand why *pak-1(tm403) spc-1(RNAi)* are shorter than *spc-1(RNAi)* embryos, we examined their elongation rate using DIC microscopy. Wild-type and *pak-1(tm403)* embryos initially elongated at the same rate, whereas *spc-1* defective embryos elongated slower and stopped around the 2-fold stage (100 µm) as previously described[19] (Fig. 2d). By contrast, *spc-1(ra409) pak-1(tm403)* and *spc-1(RNAi) pak-1(tm403)* embryos reached ≈65 µm at a slow rate, but then could not maintain their shape, retracting back to ≈50 µm, which neither *spc-1(ra409)* nor *pak-1(tm403)* embryos did (Fig. 2d, Movie 1). Two observations suggest that this phenotype is linked to muscle activity. First, *spc-1* knock-down in *git-1* or *pix-1* mutants, two other players involved in the same mechanotransduction pathway as PAK-1[9], also induced retraction (Fig. S2). Second, *spc-1(RNAi) pak-1(tm403)* embryos started to retract at the onset of active muscle contraction in control embryos (pink box in Fig. 2d). To directly prove this hypothesis, we abrogated muscle function in *spc-1(ra409) pak-1(tm403)* embryos by knocking-down the kindlin homolog UNC-112[20]. Strikingly, *spc-1(ra409) pak-1(tm403)*

93 embryos defective for *unc-112* no longer retracted (Fig. 2e; Movie 2). We conclude that
94 the mechanical input provided by muscles to the epidermis induces the retraction
95 phenotype observed in *spc-1 pak-1* double mutants.

96 The simplest interpretation of the retraction phenotype described above is that a
97 cellular structure maintaining embryo shape fails to emerge or collapses in *spc-1 pak-1*
98 double mutants once muscles become active. Two arguments lead us to consider that
99 this structure corresponds to the actin cytoskeleton. First, SPC-1/α-spectrin and its
100 binding partner SMA-1/ß-spectrin form an actin-binding hetero-tetramer colocalizing
101 with actin[21] and partially with PAK-1 in epidermal cells (Fig. S3). Second and foremost, it
102 has long been known that treating *C. elegans* embryos with the actin-depolymerizing
103 drug cytochalasin-D induces a retraction phenotype very similar to that presented
104 herein[22]. We thus characterized actin filaments by spinning-disk confocal imaging of a
105 LifeAct::GFP probe[12]. Segmentation analysis of the fluorescence signal associated with
106 actin filaments in the dorso-ventral epidermis (Fig. 3a-a''') revealed more discontinuity in
107 *spc-1 pak-1* double deficient embryos (Fig. 3d-d''') compared to the control genotypes
108 (Fig. 3a-c'''). Moreover, Fourier transform analysis indicated that their degree of
109 anisotropy relative to the circumferential axis was abnormal (Fig. 3d''-d'''). Note that
110 both phenotypes were visible mainly at mid elongation, i.e. after muscles become
111 active (Fig. S4), suggesting that a well-structured actin network emerges too slowly in
112 double mutants rather than it collapses.

113 Collectively, the results described so far, together with the retraction phenotype of
114 cytochalasin-D treated embryos[22], suggest that the actin filament defects account for
115 *spc-1 pak-1* embryo retraction, and further link muscle activity with these defects.

116 Significantly, as the wild-type embryo lengthens, its circumference decreases by roughly
117 20% due to embryo volume conservation (Fig. S5) and thus, the length of actin filaments
118 in dorso-ventral cells should decrease. Hence, we suggest that muscle activity normally
119 promotes actin filament shortening, probably through sliding or shortening of filaments
120 relative to each other after their bending (Fig. S1). We further suggest that SPC-1 and
121 PAK-1 stabilize cell shape by maintaining actin bundle integrity. We could not define the
122 shortening mechanism by spinning-disk microscopy, probably because each muscle
123 contraction results in changes beyond the time and space resolution of the microscope.
124 However, we suggest that it goes awry in the absence of SPC-1 and PAK-1, due to the
125 lack of a capping or bundling activity (Fig. 4b-b').

126 To rationalize the role of muscles in the process of actin bundle shortening and
127 stabilization, we described the *C. elegans* embryo as a Kelvin-Voigt material (a spring in
128 parallel to a dashpot) submitted to forces acting in the epidermis and muscles (F_{epid} and
129 $F_{muscles}$) (Fig. 4c equations-a and -b; Supplementary material). Note that F_{epid} is written as
130 the product of an active force, F_{seam}, and a passive component resulting from actin
131 bundle stiffness, α_{DV} (Supplementary material and ref. 11). Since muscle-defective
132 mutants cannot elongate beyond the 2-fold stage, then F_{epid} can only extend embryos
133 until that stage (due to the spring restoring force; Fig. S6a-a'). Simply adding the force
134 $F_{muscles}$ should not trigger any further extension, because it oscillates between a positive
135 and negative input (Fig. 1bc, Fig. S6b-b').

136 Recently, several studies have suggested that systems exposed to a stress can undergo
137 a permanent rearrangement, which can be described as a plastic deformation[23] or as
138 a change in the spring resting length[24,25]. Accordingly, we incorporated an increase of

the spring resting length λ in the equations described above by writing that it changes by a factor β (Fig. 4c equation-c; Fig. 4d). Thereby, we could accurately predict the elongation pattern of wild-type embryos (Fig. 4f, Fig. S6d-d'; Supplementary material). Conversely, in *spc-1 pak-1* defective embryos, the continuing damage to actin filaments should reduce their stiffness (component α_{DV} in Fig. 4c equation-b), which we expressed by writing that it depends on a tearing factor γ (Fig. 4c equation-d, Fig. 4e); thereby, we could accurately predict their retraction pattern (Fig. 4f, Fig. S6e-e'). We thus propose that SPC-1/α-spectrin and PAK-1 regulate a process of mechanical plasticity in the physical sense. From a cellular standpoint, having a changing resting length means that body elasticity does not bring the embryo back to its initial shape upon muscle relaxation, enabling progressive lengthening.

To further define the molecular basis of viscoplasticity, we performed a small-scale RNAi screen to search for gene knockdowns inducing retraction of *spc-1(ra409)* embryos (Fig. 4g; Table S3). This screen identified the atypical formin FHOD-1 (Fig. 4h-i; Fig. S7, movie 3), which has previously been linked to actin dynamics in the epidermis[26]. We confirmed that *fhod-1(tm2363); spc-1(RNAi)* embryos also showed a penetrant retraction phenotype (Fig. 4h; Fig. S7). The identification of this specific formin was intriguing because vertebrate FHOD1 promotes actin capping and bundling rather than nucleation and elongation[27]. It thus raised the tantalizing possibility that FHOD-1 activity stabilizes the actin cytoskeleton while it gets remodeled under the influence of muscle activity during embryo circumference reduction. Furthermore, the genetic interaction suggests that FHOD-1 acts with SPC-1 and PAK-1. To examine this possibility, we tested whether FHOD-1 derivatives removing at least the C-terminal DAD domain, predicted to auto-inhibit formins[28], can rescue the retraction phenotype of *spc-1 pak-1* deficient

embryos. Strikingly, after epidermis-specific expression of a form lacking the FH2 and DAD domains, transgenic *spc-1(RNAi) pak-1(tm403)* embryos did not retract and were significantly longer than non-transgenic siblings; rescue was better than with the full-length protein. By contrast, the DAD deleted form did not rescue and deletion of the FH1-FH2-DAD domains marginally rescued retraction, arguing that the FH2 F-actin nucleation domain is not necessary for rescue but that the FH1 is. Truncation of the C-terminal DAD domain or of the FH1-FH2-DAD domains marginally rescued retraction (Fig. 4j). Importantly, an FH2-DAD truncation in the mammalian FHOD1 still enables it to bundle actin[27], further strengthening the notion that FHOD-1 bundling activity is indeed required and providing a potential molecular basis for viscoplasticity. It also indicates that muscle-induced actin remodeling would primarily result from sliding and re-bundling (see Fig. 4a-a'). Furthermore, we conclude that the retraction of *spc-1 pak-1* deficient embryos mainly results from a lack of FHOD-1 activation.

Several factors could contribute to improperly regulate the activity of PAK-1 and FHOD-1. First, SPC-1 could help recruit FHOD-1 and PAK-1, since FHOD-1::GFP and PAK-1::GFP made small aggregates in SPC-1 defective embryos (Fig. S8). Second, we found that the cycles of actin filament displacement induced by muscle contractions were almost twice as short in *spc-1(RNAi) pak-1(tm403)* embryos compared to *pak-1(tm403)* and wild-type controls (3 sec against 5.7 sec; Fig. S9, Movie 4). These shorter muscle contractions might still induce actin filament shortening but not give enough time for their stabilization. Third, PAK-1 might directly activate FHOD-1 downstream of the mechanotransduction pathway induced by muscles, since *git-1* and *pix-1* mutations combined with *spc-1* RNAi-knockdown also induced a retraction (see Fig. S2a-g).

Altogether, our data identify three proteins involved in stabilizing cell shapes in a system involving two mechanically interacting tissues submitted to repeated stress. We propose that the progressive shortening of actin filaments under the control of these factors mediates a cellular viscoplastic process promoting axis elongation. A similar spectrin/p21-activated kinase/FHOD1 system might operate in vertebrate tissues comprising an epithelial layer surrounded by a contractile layer, such as our internal organs. Interestingly, high FHOD1 expression correlates with poor prognosis of breast cancer patients[29]. Thus, a similar viscoplastic process might also influence the metastatic properties of tumor cells positioned next to contractile cells.

ACKNOWLEDGEMENTS

The authors thank Anne Spang, Stephan Grill, Yohanns Bellaïche for critical comments on the manuscript, and Melanie Gettings for improving the English. We also thank the *Caenorhabditis* Genetics Center (funded by the NIH Office of Research Infrastructure Programs P40 OD010440) for strains, and the IBPS Imaging Facility for advice. This work was supported by an Agence Nationale pour la Recherche, European Research Council (grant #294744**)**, Israël-France Maïmonide exchange program grants, and installation funds from the Centre National de la Recherche Scientifique (CNRS) and University Pierre et Marie Curie (UPMC) to ML. This work was also made possible by institutional funds from the CNRS, University of Strasbourg and UPMC, the grant ANR-10-LABX-0030-INRT which is a French State fund managed by the Agence Nationale de la Recherche under the framework programme Investissements d'Avenir labelled ANR-10-IDEX-0002-02 to the IGBMC.

AUTHORS' CONTRIBUTIONS

ML conceived the project, GP initiated many aspects of the study while AL performed most experiments, with contributions from TF for modelling, TF and JP for image analysis, FL for the generation of FHOD-1 variants, CG shared data from a related screen, SK for the *spc-1(ra409)* mini-RNAi screen, DR for technical assistance. ML wrote the manuscript and all authors commented and proofread it (except SK, who was an intern), AL assembled figures, TF wrote the Supplementary mathematical modelling material, and FL the Materials section.

FIGURE LEGENDS

Figure 1: Muscle contractions deform the epidermis to their mechanical coupling

(a) *C. elegans* embryonic elongation from comma to 2-fold stages depends on a ROCK-promoted actomyosin force in seam cells (cyan) and actin-promoted stiffness in dorso-ventral cells (orange); elongation beyond the 2-fold stage requires repeated muscle contractions (red flash), which induce a PAK-1-dependent mechano-transduction pathway. Open cross-sections (bottom) show muscle positions. **(b-b''')** Epidermis actin filament (green) and muscle nucleus (red) tracking in a wild-type 2-fold embryo. **(b')** Kymographs from the yellow rectangle area (**b**) showing the concurrent

displacement of epidermal actin and muscle nuclei. **(b'')** Resulting displacement curves; **(b''')** quantification of the area between them; its low value underlines the tight mechanical coupling between both tissues. Scale bar, 10 µm. **(c-c")** A muscle contraction/relaxation cycle illustrating its local impact on epidermal actin filaments in a wild-type 2-fold embryo (timing in left corner). Yellow (relaxation), red (compression) green (stretching) distances between landmarks denoted 1-4: **(c)** [1-2], 7.8 µm; [2-3], 19.8 µm; [3-4], 24.6 µm. **(c')** [1-2], 9.4 µm; [2-3], 13.6 µm; [3-4], 26.2 µm. **(c")** [1-2], 8.0 µm; [2-3], 19.2 µm; [3-4], 25.0 µm. In (**b-c**) the *Pepidermis* promoter is *Pdpy-7*. **(d)** Hysteresis graph of an idealized elastic material returning to its initial shape after deformation (top), or showing permanent deformation[30] (bottom).

Figure 2: Loss of PAK-1 and SPC-1 triggers a muscle-dependent retraction of embryos

(a) RNAi screen in a *pak-1* mutant identified *spc-1* as an enhancer (Table S1). **(b)** DIC micrographs of newly hatched wild-type, *pak-1(tm403)* (scale bar: 10 µm), *spc-1(RNAi)* and *spc-1(RNAi) pak-1(tm403)* (scale bar: 25 µm). Quantification of L1 hatchling body length: wild-type (n=38); *pak-1(tm403) (n=32); spc-1(RNAi)(n=26); spc-1(RNAi) pak-1(tm40)* (n=36). **(c)** A yeast two-hybrid screen using the PAK-1 N-term domain as a bait identified the SPC-1 SH3 domain as a prey (orange background) (Table S2). **(d)** Elongation profiles and corresponding terminal phenotypes of wild-type (n=5), *pak-1(tm403)* (n= 5), *spc-1(RNAi)* (n=8), *spc(RNAi) pak-1(tm403)* (n=8). **(e)** Elongation profiles in a muscle defective background. *unc-112(RNAi)* (n=5); *spc-1(RNAi)* (n=8); *unc-112(RNAi); pak-1(tm403) spc-1(ra409)* (n=5); *spc-1(RNAi) pak-1(tm403)* (n=8). Right bracket (**d, e**), extent of retraction for *spc-1(RNAi) pak-1(tm403)* embryos. Scale bars, 10 µm. Error bars, SEM.

Figure 3: Actin filament defects in SPC-1 and PAK-1 defective embryos

(a-d) Epidermal actin filaments visualized with the *Pdpy-7::LifeAct::GFP* reporter construct in wild-type **(a-a''')**, *pak-1(tm403)* **(b-b''')**, *spc-1(RNAi)* **(c-c''')** and *spc-1(RNAi) pak-1(tm403)* **(d-d''')** embryos at mid-elongation (2-fold equivalent) stage. Yellow rectangle, region of interest (ROI). Scale bar, 10 µm. **(a'-d')** ROI after binarisation (green) and major axis detection (red), based on **(a''')** three steps of image treatment for continuity and orientation analysis. **(a''-d'')** Actin continuity: distribution of actin segments based on their length. Wild-type (n=16); *pak-1(tm403)* (n=21); *spc-1(RNAi)* (n=21) ; *spc-1(RNAi) pak-1(tm403)* (n=17) **(b'''-d''')** Actin filament orientation: the curves represent the number of actin filaments oriented perpendicular to the elongation axis (90° angle in wild-type) based on the Fast Fourier Transformation (FFT in a'''). Wild type (n=18) ; *pak-1(tm403)* (n=20) ; *spc-1(RNAi)* (n=18) ; *spc-1(RNAi) pak-1(tm403)* (n=18). Scale bars, 10 µm (c, d, e, f), or 1 µm (c', d', e', f'). P values, *<0,05; **<0,001; ***<0,0001; ns not significant.

Figure 4: An actin-remodeling network providing mechanical plasticity ensures embryo elongation

(a-b') Cellular model of embryo elongation. **(a-a')** In control embryos, muscle contractions (red arrows) provoke actin filament shortening in the dorso-ventral epidermis, probably through sliding or shortening, followed by SPC-1/PAK-1-dependent actin stabilization. Whether spectrin is found along (scenario 1) or between (scenario 2) actin filaments is unknown (**a**). **(b-b')** In *spc-1 pak-1* deficient embryos, actin remodeling goes uncontrolled. **(c-f)** Viscoplastic mechanical model of embryo elongation. The embryo is represented as a Kelvin-Voigt solid (spring stiffness *k*, resting length λ, viscosity

279 η) submitted to the forces F_{epid} and F_{muscle}. System equations for the model. (**d**) Wild-type
280 case: an increasing resting length during stretching phases imparts mechanical
281 plasticity. (**e**) *spc-1 pak-1* mutants: F_{epid} progressively decreases. **(f)** Comparison of
282 experimental and predicted elongation curves taking the constitutive equations shown
283 in (**c**). **(g)** A retraction screen in a *spc-1* mutant identifies *fhod-1*. **(h)** Snapshot at three
284 time-points of *spc-1* deficient embryos in control, *pak-1* or *fhod-1* backgrounds; **(i)**
285 terminal body length at hatching: *spc-1(ra409)* after feeding on L4440 control (n=21), or
286 *fhod-1(RNAi)* (n=25) bacteria. **(j)** *Pdpy-7* driven epidermis expression of truncated FHOD-
287 1 variants and terminal body length at hatching: *spc-1(RNAi)*(n=26); *spc-1(RNAi)pak-*
288 *1(tm403)* no transgene (n=36), FHOD-1(full length) (n=16), FHOD-1(ΔDAD) (n=17), FHOD-
289 1(ΔFH2-DAD) (n=38) and non-transgenic siblings (n=78), FHOD-1(ΔFH1-FH2-DAD) (n=18).
290 Scale bar, 15 µm. Error bars, SEM. P values: *<0,05; **<0,001; ***<0,0001; ns, not significant.
291
292
293

References

1 Tada, M. & Heisenberg, C. P. Convergent extension: using collective cell migration and cell intercalation to shape embryos. *Development* **139**, 3897-3904, doi:10.1242/dev.073007 (2012).

2 Gilmour, D., Rembold, M. & Leptin, M. From morphogen to morphogenesis and back. *Nature* **541**, 311-320, doi:10.1038/nature21348 (2017).

3 Keller, R. Developmental biology. Physical biology returns to morphogenesis. *Science* **338**, 201-203, doi:10.1126/science.1230718 (2012).

4 Martin, A. C., Kaschube, M. & Wieschaus, E. F. Pulsed contractions of an actin-myosin network drive apical constriction. *Nature* **457**, 495-499, doi:nature07522 [pii]
10.1038/nature07522 (2009).

5 Rauzi, M., Lenne, P. F. & Lecuit, T. Planar polarized actomyosin contractile flows control epithelial junction remodelling. *Nature* **468**, 1110-1114, doi:nature09566 [pii]
10.1038/nature09566 (2010).

6 Collinet, C., Rauzi, M., Lenne, P. F. & Lecuit, T. Local and tissue-scale forces drive oriented junction growth during tissue extension. *Nat Cell Biol* **17**, 1247-1258, doi:10.1038/ncb3226 (2015).

7 Desprat, N., Supatto, W., Pouille, P. A., Beaurepaire, E. & Farge, E. Tissue deformation modulates twist expression to determine anterior midgut differentiation in Drosophila embryos. *Dev Cell* **15**, 470-477, doi:10.1016/j.devcel.2008.07.009 (2008).

8 Lye, C. M. *et al.* Mechanical Coupling between Endoderm Invagination and Axis Extension in Drosophila. *PLoS Biol* **13**, e1002292, doi:10.1371/journal.pbio.1002292 (2015).

9 Zhang, H. *et al.* A tension-induced mechanotransduction pathway promotes epithelial morphogenesis. *Nature* **471**, 99–103, doi:10.1038/nature09765 (2011).

10 Behrndt, M. *et al.* Forces driving epithelial spreading in zebrafish gastrulation. *Science* **338**, 257-260, doi:10.1126/science.1224143 (2012).

11 Dierkes, K., Sumi, A., Solon, J. & Salbreux, G. Spontaneous oscillations of elastic contractile materials with turnover. *Phys Rev Lett* **113**, 148102, doi:10.1103/PhysRevLett.113.148102 (2014).

12 Vuong-Brender, T. T., Ben Amar, M., Pontabry, J. & Labouesse, M. The interplay of stiffness and force anisotropies drive embryo elongation. *Elife* **6**, doi:10.7554/eLife.23866 (2017).

13 Munro, E., Nance, J. & Priess, J. R. Cortical flows powered by asymmetrical contraction transport PAR proteins to establish and maintain anterior-

posterior polarity in the early C. elegans embryo. *Developmental cell* **7**, 413-424, doi:10.1016/j.devcel.2004.08.001 (2004).
14 Vuong-Brender, T. T., Yang, X. & Labouesse, M. C. elegans Embryonic Morphogenesis. *Curr Top Dev Biol* **116**, 597-616, doi:10.1016/bs.ctdb.2015.11.012 (2016).
15 Simoes Sde, M., Mainieri, A. & Zallen, J. A. Rho GTPase and Shroom direct planar polarized actomyosin contractility during convergent extension. *The Journal of cell biology* **204**, 575-589, doi:10.1083/jcb.201307070 (2014).
16 Vasquez, C. G., Tworoger, M. & Martin, A. C. Dynamic myosin phosphorylation regulates contractile pulses and tissue integrity during epithelial morphogenesis. *The Journal of cell biology* **206**, 435-450, doi:10.1083/jcb.201402004 (2014).
17 Gally, C. *et al.* Myosin II regulation during C. elegans embryonic elongation: LET-502/ROCK, MRCK-1 and PAK-1, three kinases with different roles. *Development* **136**, 3109-3119, doi:10.1242/dev.039412 (2009).
18 Vuong-Brender, T. T. K., Suman, S. K. & Labouesse, M. The apical ECM preserves embryonic integrity and distributes mechanical stress during morphogenesis. *Development*, doi:10.1242/dev.150383 (2017).
19 Norman, K. R. & Moerman, D. G. Alpha spectrin is essential for morphogenesis and body wall muscle formation in Caenorhabditis elegans. *The Journal of cell biology* **157**, 665-677, doi:10.1083/jcb.200111051 (2002).
20 Rogalski, T. M., Mullen, G. P., Gilbert, M. M., Williams, B. D. & Moerman, D. G. The UNC-112 gene in Caenorhabditis elegans encodes a novel component of cell-matrix adhesion structures required for integrin localization in the muscle cell membrane. *The Journal of cell biology* **150**, 253-264 (2000).
21 Praitis, V., Ciccone, E. & Austin, J. SMA-1 spectrin has essential roles in epithelial cell sheet morphogenesis in C. elegans. *Dev Biol* **283**, 157-170 (2005).
22 Priess, J. R. & Hirsh, D. I. *Caenorhabditis elegans* morphogenesis: the role of the cytoskeleton in elongation of the embryo. *Dev Biol* **117**, 156-173 (1986).
23 Bonakdar, N. *et al.* Mechanical plasticity of cells. *Nat Mater* **15**, 1090-1094, doi:10.1038/nmat4689 (2016).
24 Doubrovinski, K., Swan, M., Polyakov, O. & Wieschaus, E. F. Measurement of cortical elasticity in Drosophila melanogaster embryos using ferrofluids. *Proc Natl Acad Sci U S A* **114**, 1051-1056, doi:10.1073/pnas.1616659114 (2017).
25 Munoz, J. J. & Albo, S. Physiology-based model of cell viscoelasticity. *Phys Rev E Stat Nonlin Soft Matter Phys* **88**, 012708, doi:10.1103/PhysRevE.88.012708 (2013).
26 Vanneste, C. A., Pruyne, D. & Mains, P. E. The role of the formin gene fhod-1 in C. elegans embryonic morphogenesis. *Worm* **2**, e25040, doi:10.4161/worm.25040 (2013).

27 Schonichen, A. *et al.* FHOD1 is a combined actin filament capping and bundling factor that selectively associates with actin arcs and stress fibers. *J Cell Sci* **126**, 1891-1901, doi:10.1242/jcs.126706 (2013).
28 Kuhn, S. & Geyer, M. Formins as effector proteins of Rho GTPases. *Small GTPases* **5**, e29513, doi:10.4161/sgtp.29513 (2014).
29 Jurmeister, S. *et al.* MicroRNA-200c represses migration and invasion of breast cancer cells by targeting actin-regulatory proteins FHOD1 and PPM1F. *Mol Cell Biol* **32**, 633-651, doi:10.1128/MCB.06212-11 (2012).
30 Vincent, J. in *Structural Biomaterials: Third Edition* 1-28 (Princeton University Press, 2012).

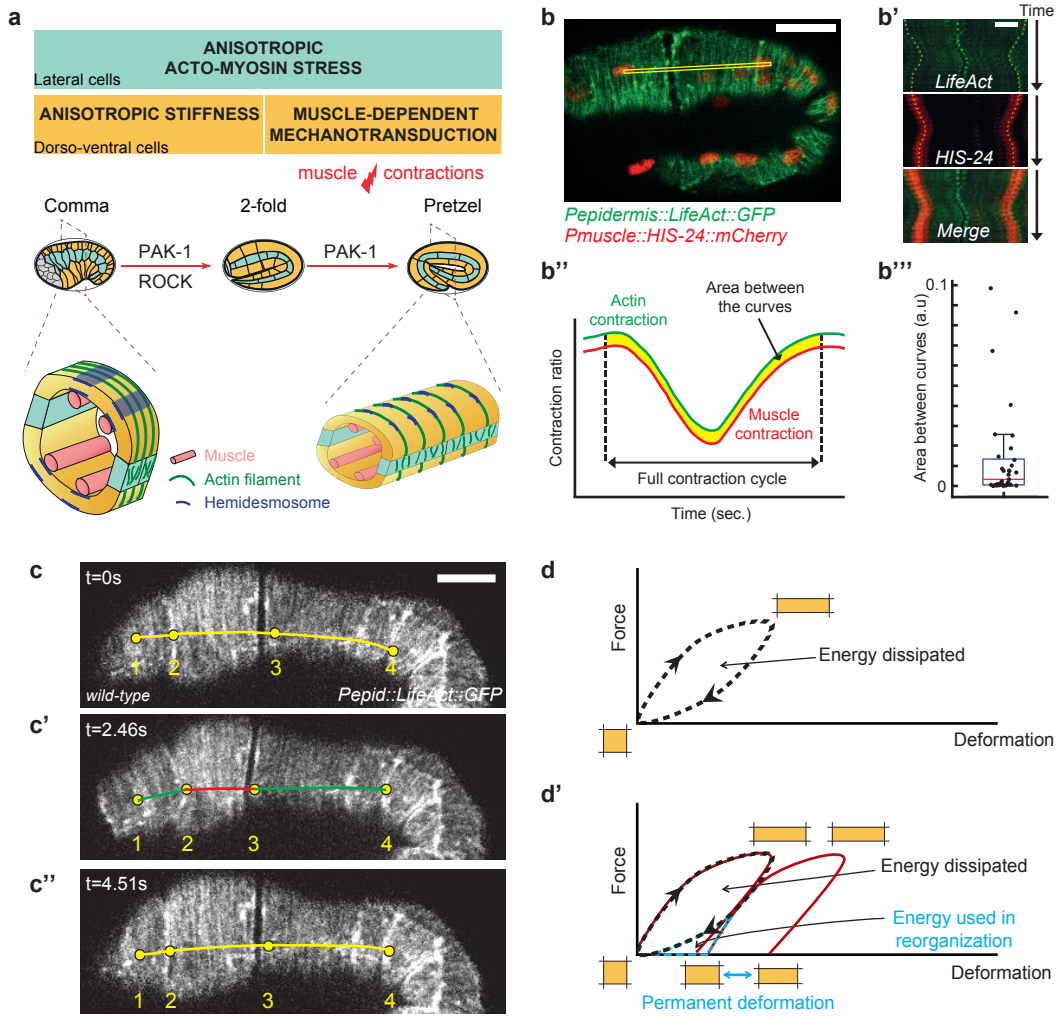

Figure 1: Muscle contractions deform the epidermis to their mechanical coupling

(a) C. elegans embryonic elongation from comma to 2-fold stages depends on a ROCK-promoted actomyosin force in seam cells (cyan) and actin-promoted stiffness in dorso-ventral cells (orange); elongation beyond the 2-fold stage requires repeated muscle contractions (red flash), which induce a PAK-1-dependent mechano-transduction pathway. Open cross-sections (bottom) show muscle positions.
(b-b''') Epidermis actin filament (green) and muscle nucleus (red) tracking in a wild-type 2-fold embryo.
(b') Kymographs from the yellow rectangle area (b) showing the concurrent displacement of epidermal actin and muscle nuclei.
(b'') Resulting displacement curves;
(b''') quantification of the area between them; its low value underlines the tight mechanical coupling between both tissues. Scale bar, 10 µm.
(c-c") A muscle contraction/relaxation cycle illustrating its local impact on epidermal actin filaments in a wild-type 2-fold embryo (timing in left corner). Yellow (relaxation), red (compression) green (stretching) distances between landmarks denoted 1-4:
(c) [1-2], 7.8 µm; [2-3], 19.8 µm; [3-4], 24.6 µm.
(c') [1-2], 9.4 µm; [2-3], 13.6 µm; [3-4], 26.2 µm.
(c") [1-2], 8.0 µm; [2-3], 19.2 µm; [3-4], 25.0 µm.
In (b-c) the Pepidermis promoter is Pdpy-7.
(d) Hysteresis graph of an idealized elastic material returning to its initial shape after deformation (top), or showing permanent deformation30 (bottom).

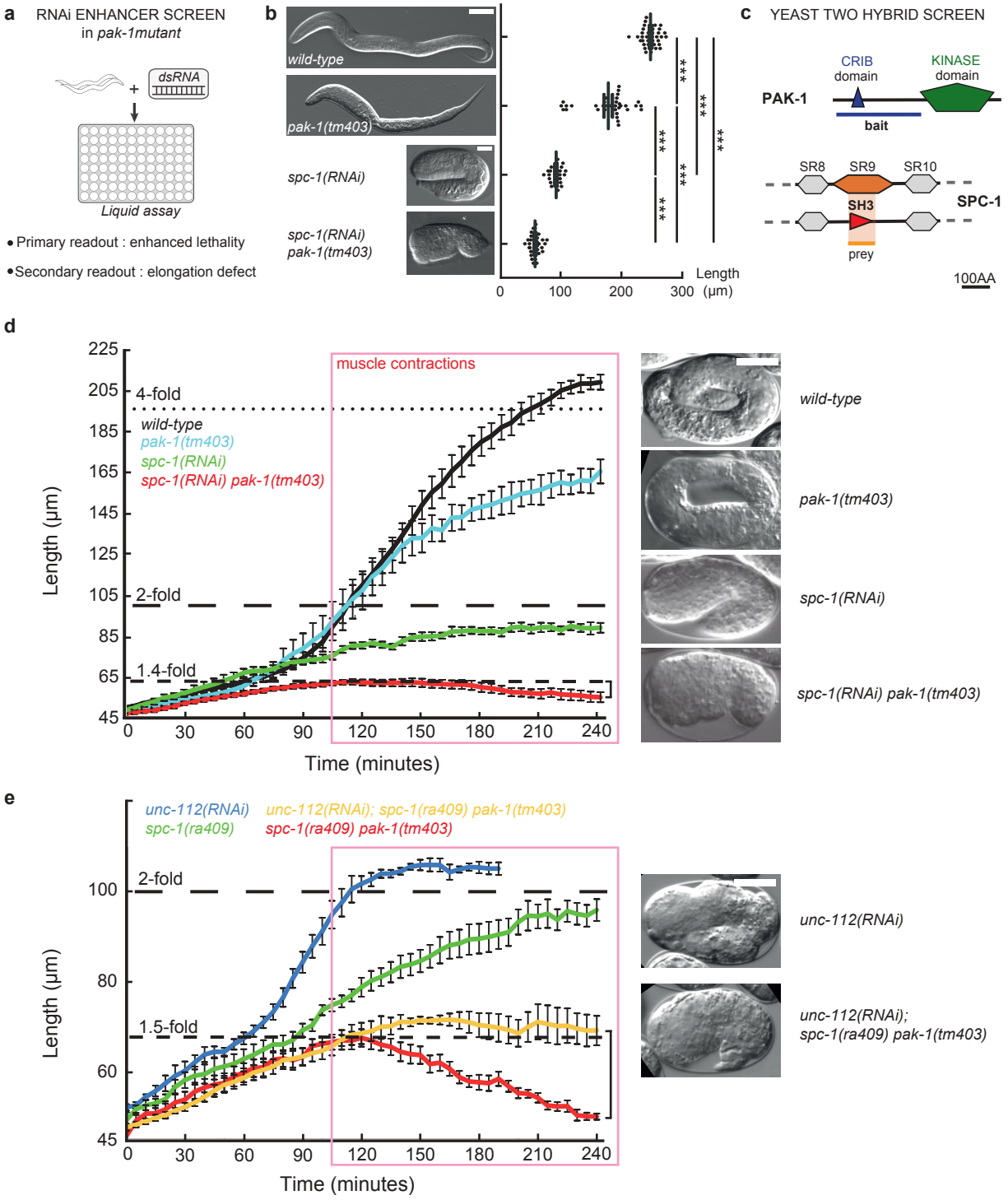

Figure 2: Loss of PAK-1 and SPC-1 triggers a muscle-dependent retraction of embryos

(a) RNAi screen in a pak-1 mutant identified spc-1 as an enhancer (Table S1).
(b) DIC micrographs of newly hatched wild-type, pak-1(tm403) (scale bar: 10 µm), spc-1(RNAi) and spc-1(RNAi) pak-1(tm403) (scale bar: 25 µm).
Quantification of L1 hatchling body length: wild-type (n=38); pak-1(tm403) (n=32); spc-1(RNAi)(n=26); spc-1(RNAi) pak-1(tm40) (n=36).
(c) A yeast two-hybrid screen using the PAK-1 N-term domain as a bait identified the SPC-1 SH3 domain as a prey (orange background) (Table S2).
(d) Elongation profiles and corresponding terminal phenotypes of wild-type (n=5), pak-1(tm403) (n= 5),
spc-1(RNAi) (n=8), spc(RNAi) pak-1(tm403) (n=8).
(e) Elongation profiles in a muscle defective background.
unc-112(RNAi) (n=5); spc-1(RNAi) (n=8); unc-112(RNAi); pak-1(tm403) spc-1(ra409) (n=5); spc-1(RNAi) pak-1(tm403) (n=8).
Right bracket (d, e), extent of retraction for spc-1(RNAi) pak-1(tm403) embryos. Scale bars, 10 µm. Error bars, SEM.

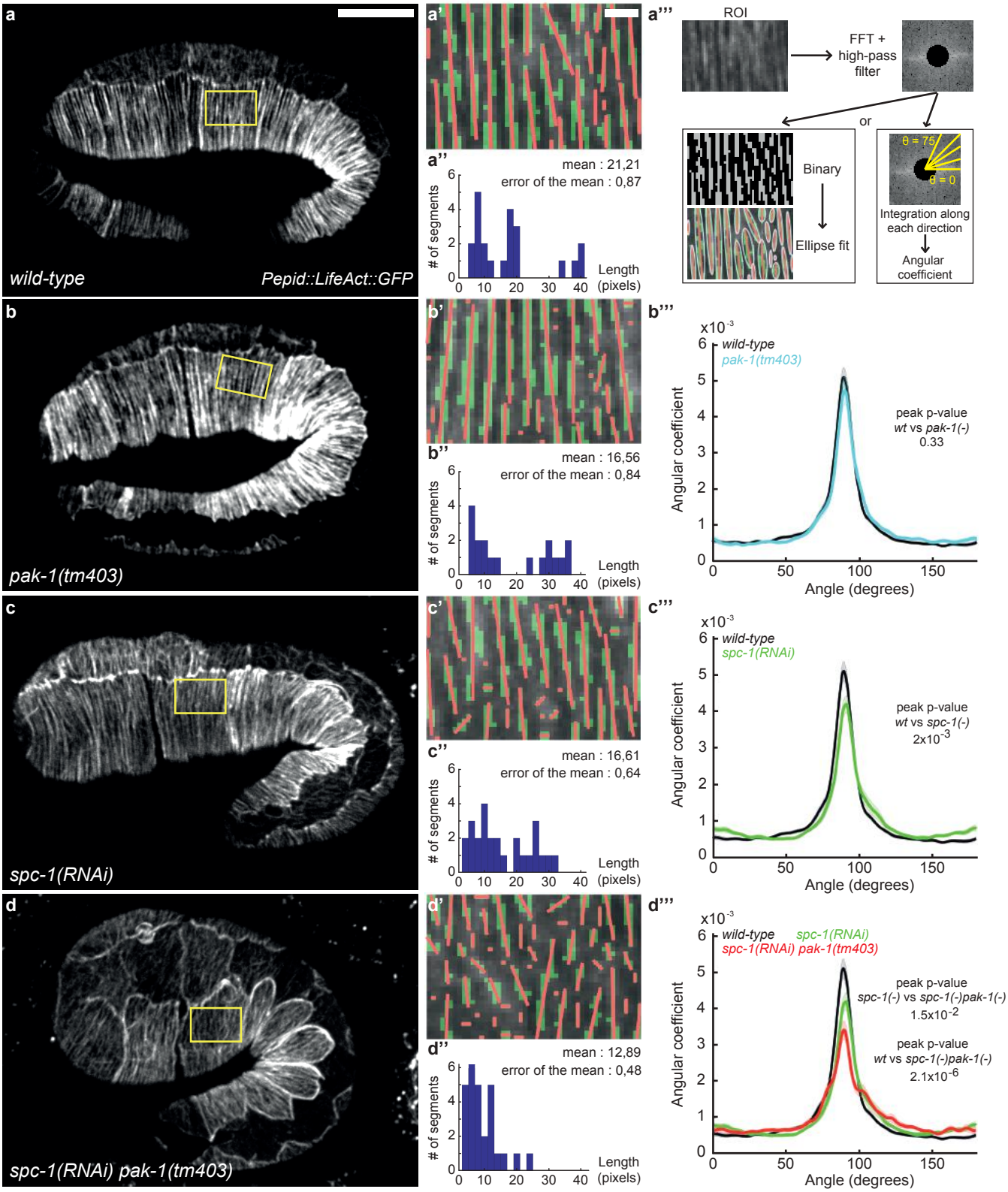

Figure 3: Actin filament defects in SPC-1 and PAK-1 defective embryos

(a-d) Epidermal actin filaments visualized with the Pdpy-7::LifeAct::GFP reporter construct in wild-type (a-a'''), pak-1(tm403) (b-b'''), spc-1(RNAi) (c-c''') and spc-1(RNAi) pak-1(tm403) (d-d''') embryos at mid-elongation (2-fold equivalent) stage.
Yellow rectangle, region of interest (ROI). Scale bar, 10 µm.
(a'-d') ROI after binarisation (green) and major axis detection (red),
based on (a''') three steps of image treatment for continuity and orientation analysis.
(a''-d'') Actin continuity: distribution of actin
segments based on their length. Wild-type (n=16); pak-1(tm403) (n=21); spc-1(RNAi) (n=21) ; spc-1(RNAi) pak-1(tm403) (n=17)
(b'''-d''') Actin filament orientation: the curves represent the number of actin filaments oriented perpendicular to the elongation axis (90° angle in wild-type) based on the Fast Fourier Transformation (FFT in a''').
Wild type (n=18) ; pak-1(tm403) (n=20) ; spc-1(RNAi) (n=18) ; spc-1(RNAi) pak-1(tm403) (n=18).
Scale bars, 10 µm (c, d, e, f), or 1 µm (c', d', e', f'). P values, *<0,05; **<0,001; ***<0,0001; ns not significant.

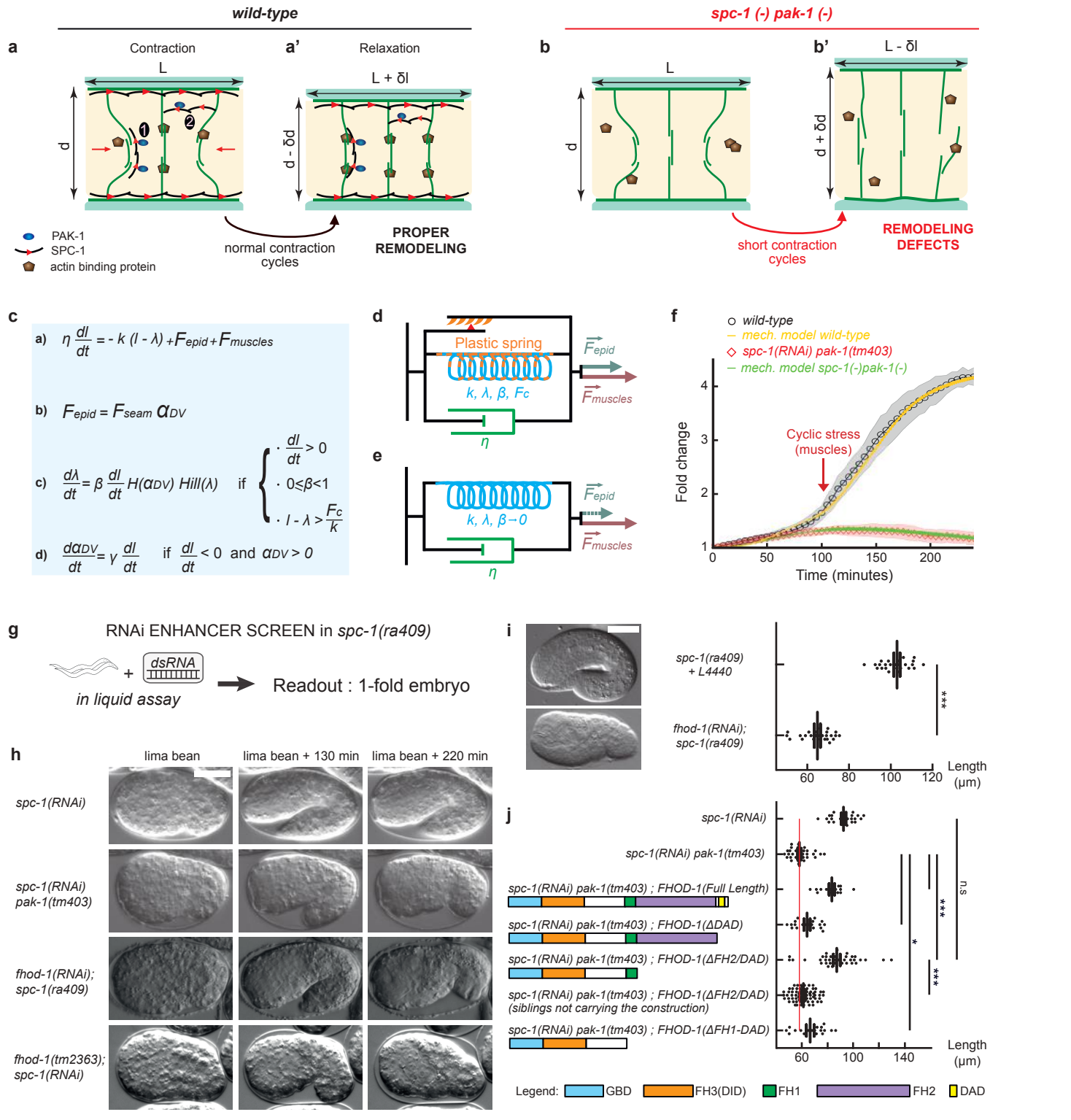

Figure 4: An actin-remodeling network providing mechanical plasticity ensures embryo elongation

(a-b') Cellular model of embryo elongation.
(a-a') In control embryos, muscle contractions (red arrows) provoke actin filament shortening in the dorso-ventral epidermis, probably through sliding or shortening, followed by SPC-1/PAK-1-dependent actin stabilization. Whether spectrin is found along (scenario 1) or between (scenario 2) actin filaments is unknown (a). (b-b') In spc-1 pak-1 deficient embryos, actin remodeling goes uncontrolled.
(c-f) Viscoplastic mechanical model of embryo elongation. The embryo is represented as a Kelvin-Voigt solid (spring stiffness k, resting length λ, viscosity η) submitted to the forces Fepid and Fmuscle. System equations for the model.
(d) Wild-type case: an increasing resting length during stretching phases imparts mechanical plasticity.
(e) spc-1 pak-1 mutants: Fepid progressively decreases.
(f) Comparison of experimental and predicted elongation curves taking the constitutive equations shown in (c).
(g) A retraction screen in a spc-1 mutant identifies fhod-1.
(h) Snapshot at three time-points of spc-1 deficient embryos in control, pak-1 or fhod-1 backgrounds;
(i) terminal body length at hatching: spc-1(ra409) after feeding on L4440 control (n=21), or fhod-1(RNAi) (n=25) bacteria.
(j) Pdpy-7 driven epidermis expression of truncated FHOD-1 variants and terminal body length at hatching: spc-1(RNAi)(n=26); spc-1(RNAi)pak-1(tm403) no transgene (n=36), FHOD-1(full length) (n=16), FHOD-1(ΔDAD) (n=17), FHOD-1(ΔFH2-DAD) (n=38) and non-transgenic siblings (n=78), FHOD-1(ΔFH1-FH2-DAD) (n=18). Scale bar, 15 μm. Error bars, SEM. P values: *<0,05; **<0,001; ***<0,0001; ns, not significant.

SUPPLEMENTARY MATERIAL

An actin-based viscoplastic lock ensures progressive body axis elongation

Alicia Lardennois[1]*, Gabriella Pásti[2]*, Teresa Ferraro[1], Julien Pontabry[2,3], David Rodriguez[2], Samantha Kim[2], Flora Llense[1], Christelle Gally[2], Michel Labouesse[1,2] #

Content

1-Supplementary Mechanical Modeling

1.1 Background information. During embryogenesis the *C. elegans* embryo undergoes a process of elongation whereby it becomes four times as long as the long axis of the eggshell (50 µm). Cell proliferation and cell intercalation are absent, therefore the process of axis elongation relies only on the ability of the embryo to extend in the anterior-posterior direction. The outer epithelium (epidermis) plays an essential role in this process.

Changing the status of any physical entity requires the involvement of a force (mechanical or chemical), and the *C. elegans* embryo is no exception to this rule of physics. During the first phase of elongation and until muscles become active, the

machinery driving elongation involves an active force in the lateral epidermis (also called seam cells), and a passive force exerted by the dorsal and ventral epidermal cells (called DV cells) adjacent to the seam cells (Fig. 1a). Seam cells have a high concentration of non-muscle myosin II, which has a non-polarized distribution and does not display pulsatile flows[1,2], as observed for instance during *Drosophila* germband elongation[3]. Nevertheless, the stress generated by the seam cells is anisotropic and globally oriented along the DV axis (see cyan box in Fig. 1a)[2]. The stress anisotropy results mainly from the presence of circumferential F-actin filament bundles in DV epidermal cells, which create a global stiffness anisotropy (see yellow box in Fig. 1a). The DV epidermal cells do not contribute to generate active stress (Fig. 1a), as their myosin II is kept mostly silent through the activity of the RhoGAP RGA-2[1,2,4]. The interplay between stress anisotropy in seam cells, stiffness anisotropy from the DV epidermis, and hydrostatic pressure resulting from the reduction of embryo diameter, induces a force oriented along the AP direction that is sufficient to extend the embryo until it reaches the 2-fold stage[2].

Note that here as well as in the main text we refer to each elongation phase based on the ratio between the actual embryo length and that of the eggshell long axis, i.e. 1.7-fold or 2-fold means that the embryo has reached roughly 85 µm or 100 µm, respectively. Importantly, in mutant embryos which extend slower, we refer to embryo stages based on the length that a wild-type embryo would reach after the same time duration with t_0 corresponding to the beginning of elongation (see extension curves in Fig. 2d and Movie 1).

For simplicity, let us call the net force in the AP direction produced by the epidermis the epidermal cell force (F_{epid}). This force is not enough to explain the elongation up to the 4-fold stage, since genetic analysis has established that embryos with non-

functional muscles do not elongate beyond the 2-fold stage (Fig. 2b)[5]. Therefore, muscles provide a second active force driving elongation beyond the 2-fold stage, which we will call $F_{muscles}$.

During embryogenesis, muscles organize and assemble in four rows located under the epidermis (Fig. 1a). Muscles are attached to the extracellular matrix that separates them from the epidermis, and that in turn serves to anchor the epidermis through hemidesmosome-like junctions[1]. Muscle organization and maturation is a progressive process, such that muscle activity starts with small contractions at the 1.7-fold, which progressively become more robust. The mechanical activity of muscles can be summarized as an alternation of contractions followed by relaxation. Since muscles are tightly connected to the epidermis, their contractions locally and repeatedly induce an anterior-posterior compression and extension of the epidermis, which can be visualized through the displacement of the actin cables (Fig. 1b-c, Fig. S7). The stress exerted by muscle contractions on the epidermis induces a mechanotransduction pathway (2nd yellow box in Fig. 1a), which is essential to promote hemidesmosome maturation and embryo elongation[8].

1.2 Viscoplastic model. The *C. elegans* epidermis can be modelled as a visco-elastic body, more specifically as a Kelvin-Voigt system with a spring and dashpot in parallel, subject to two main active forces: the epidermal force F_{epid}, which is a continous positive force, and the muscle force $F_{muscles}$, which is a pulsatile force since muscles alternatively contract and relax. The first force is present since the beginning of elongation, whereas the second force starts only after the 1.7-fold stage. The elastic reaction of the epidermis to active forces can be captured by Hooke's law; the damped nature of the reaction can be expressed by a viscous term. Overall the

length of the embryo over time *l(t)* can be captured by the equation:

$$\eta \frac{dl}{dt} = -k\,(l-\lambda) + F_{epid} + F_{muscles} \quad (1)$$

where *k* is the body stiffness, λ is the worm resting length and η is the coefficient of viscosity. Inertia has been neglected given the low Reynolds number of the system. Eq. (1) corresponds to the so-called Kelvin-Voigt viscoelastic model[6,7] that captures the behavior of viscoelastic solids under stress or deformation. For constant forces, the solution of Eq. (1) is given by:

$$l(t) = \frac{F_{epid} + F_{muscles}}{k}\,(1 - e^{-t/\tau}) + \lambda \quad (2)$$

meaning that the length of the system relaxes to the plateau value $\frac{F_{epid} + F_{muscles}}{k}$ in a relaxation time of $\tau = \eta/k$.

F_{epid} can promote elongation until the 2-fold stage (Fig. S5a'). Beyond, the pulsatile force originating from muscles, $F_{muscles}$, alternates periods of positive, negative or null contribution, so that its temporal average $< F_{muscles} >_\theta$ is null:

$$< F_{muscles} >_\theta = \frac{1}{\theta}\int_0^\theta F_{muscles}(t)\ dt = 0, \text{for } \theta = nT \quad (3)$$

where θ is the integration period, *T* is the period and n is a positive integer. As a consequence, on average, $F_{muscles}$ will not contribute to the steady state length (l_{ss}) of the embryo (see Fig. S5a-c) that is set by $l_{ss} = \frac{F_{epid}}{k} + \lambda$.

A way to introduce a positive contribution to embryo lengthening is to allow some plasticity, in the physical sense, or ability of the system to get reorganized. For example, let consider a stretching pulse due to muscle activity during which the embryo increases its length *l(t)* with an increment *dl*, such that the embryo will be

temporarily *l(t)+dl* long at the end of the pulse. During the subsequent relaxation phase, due to elasticity in the system, the embryo should return to the initial length *l(t)* it had before muscles had locally extended it. However, if it undergoes a permanent plastic deformation, then the body will permanently keep a portion of the stretched length. This situation corresponds to a permanent rearrangement, and it has been observed and modeled in biological systems undergoing stresses[8,9]. Similarly to[9], a simple mathematical solution to introduce plasticity consists in having an adjustable resting length λ that increases linearly with the length *l(t)* according to:

$$\frac{d\lambda}{dt} = \beta \frac{dl}{dt} \mathrm{H}(\alpha_{DV}) \quad \text{if } \frac{dl}{dt} > 0 \text{ and } l - \lambda > {}^{F_c}/_{k} \tag{4}$$

where 0≤β<1 is a proportionality factor called 'plasticity factor'; the case of β=0 corresponds to an absence of plasticity. The condition $\frac{dl}{dt} > 0$ ensures that there is rearrangement only during the extension phases and the condition; $l - \lambda > {}^{F_c}/_{k}$ means that the rearrangement takes place only if the applied force exceeds a critical force F_c. The term $\mathrm{H}(\alpha_{DV})$ is the Haeviside step function, which expresses that dorso-ventral rearrangement is possible only in presence of resistance. For the description of α_{DV} term, see next paragraph. Note that Eq. (4) is equivalent to $\lambda = \lambda(0)\,(1-\beta) + \beta\, l$ with $\lambda(0)$ being both the length and the resting length at time zero and $F_c = 0$. With these choices and with a constant positive force *F* Eq. (1) has the following solution:

$$l(t) = \frac{1}{(1-\beta)} \frac{F}{k} (1 - e^{-t(1-\beta)/\tau}) + \lambda(0) \tag{5}$$

Hence, the plasticity condition effectively reduces the body stiffness k to $k(1-\beta)$ enabling the system to reach a longer final size compared to the one allowed by the Kelvin-Voigt system alone, and increasing the relaxation time. By introducing

plasticity like in Eq. (4), the body progressively gains length at each stretching phase (Fig S5d-d').

1.3 The consequences of actin stability defects. As reminded above, the intensity of F_{epid} relies on two components: the constant contractility of the seam cell actomyosin network, and the stiffness of the actin cables in DV cells. We can then represent it like:

$$F_{epid} = F_{seam}\ \alpha_{DV} \quad (6)$$

where the force F_{seam} represents the active force generated by myosin II in the lateral cells and α_{DV} is the passive component given by the presence of actin filament bundles in the DV cells. The biomechanical significance of equation (6) is that both F_{seam} and α_{DV} positively contribute to F_{epid}, and that if one is absent $F_{epid}=0$. This captures the fact that in the absence of myosin II there will be no pulling force because the active component is absent, and that if actin cables are lost myosin II is missing the resistance structure onto which it can pull, resulting in a null epidermis AP force.

As shown in the main text (Fig. 3), the absence of SPC-1 and PAK-1, combined with the mechanical input from muscles, induces actin integrity defects in DV cells. To translate this situation in mathematical terms, we chose to write the passive component α_{DV} as follows:

$$\frac{d\alpha_{DV}}{dt} = \gamma \frac{dl}{dt} \quad if \quad \frac{dl}{dt} < 0 \ \textit{and}\ \alpha_{DV} \geq 0 \quad (7)$$

where $\gamma \geq 0$ is a proportionality factor defined as a 'tearing factor'. The condition

$\frac{dl(t)}{dt} < 0$ means that α_{DV} decreases stepwise with time. In addition, we are imposing that γ=0 corresponds to an absence of tearing, like in wild-type embryos. The biological significance of this choice is the following: in phases of length decrease (net negative force), the overall circumference of the embryo should increase due to volume conservation (Fig. S4). In a background of unstable actin filaments (like in *spc-1 pak-1* double mutants) their resistance to stress originating from muscle activity would not be maintained. For this reason, α_{DV} should progressively decrease at each cycle. The condition $\alpha_{DV} \geq 0$ prevents α_{DV} from assuming negative values. Thus with α_{DV} decreasing, F_{epid} will progressively decrease, and as consequence the system length will shorten (see Fig. S5e and Fig. 4e).

1.4 Equations summary. In summary, we describe the embryo body as a plastic Kelvin-Voigt solid according to the following system of equations:

$$\eta \frac{dl}{dt} = -k\,(l-\lambda) + F_{epid} + F_{muscles} \qquad (1)$$ (Kelvin-Voigt with adjusting resting length subject to F_{epid}+$F_{muscles}$)

$$\frac{d\lambda}{dt} = \beta \frac{dl}{dt} \mathrm{H}(\alpha_{DV}) \qquad \text{if } \frac{dl}{dt} > 0\,,\ 0 \leq \beta < 1 \text{ and } l-\lambda > {}^{F_c}/_{k} \qquad (5)$$ (plasticity condition)

$$\frac{d\alpha_{DV}}{dt} = \gamma \frac{dl}{dt} \quad if \ \frac{dl}{dt} < 0 \ and \ \alpha_{DV} \geq 0 \qquad (7)$$ (tearing condition)

With $F_{epid} = F_{seam}\ \alpha_{DV}$ as described in Eq.(4).

We assume that γ=0 for wild-type and *unc-112*, meaning that the resistance of dorso-ventral actin filament bundles remains unaffected by the body length changes caused by muscle activity.

The equations (1), (4), (5) and (7) have seven parameters: η, k, F_{seam}, $\alpha_{DV}(0)$, $F_{muscles}$, β and γ. In order to reduce the parameter space we fixed some of them:

- for simplicity we set **k=1**;
- from the laser ablation experiments performed in reference[2], the relaxation time of epidermal actin filaments following the laser cut is in the order of a few seconds. Being the relaxation time in a Kelvin-Voigt system given by $\tau = \eta/k$, we set $\boldsymbol{\eta}$**=3** so that the relaxation time is 3 seconds.
- F_{epid} is the multiplication of two parameters, and thus from the parameter point of view can be considered as a single parameter that we formally set to $\boldsymbol{F_{seam}}$**=1** letting $\alpha_{DV}(0)$ as a free parameter.
- The size of the critical force F_c has been chosen to be half F_{seam} ($\boldsymbol{F_c = 0.5}$). Thereby, we consider that low intensity forces cannot trigger a plastic response.
- Regarding $F_{muscles}$, we specified its details on the basis of the measured contraction durations for embryos between 1.7 and 2-fold stages (Fig. S7). For wild-type embryos, the duration of positive and negative periods has been set to 6 seconds and the period of null contribution has been set to 15 seconds, whereas for *spc-1* mutants and *spc-1 pak-1* double mutants the duration of non-null activity has been set to 3 seconds and the duration of null contribution is set to 15 seconds. In wild-type embryos, the intensity of $F_{muscles}$ has been left as a fit parameter together with α_{DV}, β and γ in order to be determined by comparing with the data. The muscle force amplitude for *spc-1* and *spc-1 pak-1* mutants has been set to **50% of the *wt* intensity** according to our experimental observations.

To better adapt to the experimental observations, both F_{seam} and $F_{muscles}$ have been modified by introducing an initial transient that sets their behavior from zero to the

187 regime of maximal intensity; the detailed form of these transients are reported in the
188 paragraph 'Refining model details'.

189

190 **1.5 Fitting procedure.** In order to determine the remaining four free parameters:
191 intensity of $F_{muscles}$, $\alpha_{DV}(0)$ (the initial value of actin strength), β (the plasticity factor)
192 and γ (tearing factor) we fitted different genotypes. We started with the muscle-
193 defective *unc-112* and wild-type embryos. As shown in Figs. 2 and S3, their
194 elongation rate is quite similar until the 2-fold stage, at which point *unc-112* embryos
195 have no muscle force ($F_{muscles}$=0), and they both have an identical actin pattern
196 (γ=0). Therefore, we fitted together the two elongation curves to find the values of
197 the three parameters $\alpha_{DV}(0)$, β and $F_{muscles}$ that capture the main features of the two
198 genotypes, and we refined the minor differences by allowing a 20% tolerance with
199 respect to the parameters values determined through the common fit. To estimate
200 the value of $F_{muscles}$ intensity in *spc-1* and *spc-1 pak-1* embryos, we considered that it
201 was half the wild-type value, based on the observation that the muscle
202 contraction/relaxation cycles were roughly twice shorter in these embryos (Fig. S7).
203 The notion that $F_{muscles}$ is lower in *spc-1* mutant embryos is consistent with the
204 observation that muscles make an angle of 20° with the anterior-posterior axis,
205 instead of 6° in wild-type embryos, predicting that their input should be reduced[10].
206 The wild-type value of the plasticity factor was used as the upper limit for the
207 variability range of β for *spc-1* and *spc-1 pak-1* embryos. We then proceeded by
208 fitting the *spc-1* and *spc-1 pak-1* elongation curves to determine the values of
209 $\alpha_{DV}(0)$, β and the tearing factor γ (see below for the method).

210 The best fit parameters were determined by minimalizing the following cost function:

$$\xi = \sum_g \sum_i [(curve_{data}(i) - curve_{model}(i))^2]_g \quad (8)$$

where $curve_{data}(i)$ is the value of the data elongation curve at the time point i and $curve_{model}(i)$ is the solution of the model interpolated at the time point i; g refers to the genotypes cosidered for a fit. To minimize the cost function, a Covariance Matrix Adaptation Evolution Strategy (CMA-ES) algorithm was used[11]. The algorithm has an available Matlab code at http://www.lri.fr/~hansen/cmaes_inmatlab.html.

In the following table we report the values of the fitted parameters for the different genotypes presented in the Fig. 4j and S5f. Errors have been obtained by fitting the mean curves plus and minus their standard errors respectively and by taking the maximal deviation from the parameters obtained from the mean.

	wild-type	*unc-112*	*spc-1*	*spc-1 pak-1*
Initial actin stiffness $\alpha_{DV}(0)$	1.06 ± 0.05	1.13 ± 0.01	0.84 ± 0.03	0.76 ± 0.03
Plasticity factor β	0.12 ± 0.06	0.05 ± 0.01	0.06± 0.02	0.02± 0.03
Intensity $F_{muscles}$	5.0 ± 2.5	∅	2.5	2.5
Tearing factor γ	∅	∅	0.04± 0.01	0.12 ± 0.01

1.6 Refining model details. Ablation experiments in seam cells[2] have shown that the circumferential stress is not constant during development but increases from the 1.3-fold to 1.7-fold stages. To better adapt our model to this observation, we introduced a time dependent function for F_{epid} that saturates to a plateau value within a time τ_s :

$$F_{epid}(t) = F_{seam}\ \alpha_{DV}\ (1 - \exp\left(-\frac{t}{\tau_s}\right))^{h_s} \quad (9)$$

where h_s is an exponent that sets the steepness of the function in reaching the plateau and $F_{seam}\ \alpha_{DV}$ is the plateau value. We set τ_s=*50* min and h_s=*4*, since this choice produces slow elongation for the first 50 minutes, as was observed for all the genotypes (see Fig. 2). Much like the epidermis force, the muscle force $F_{muscles}$ also starts at a small amplitude, then progressively evolves with a behavior similar to equation (8):

$$F_{muscles}(t) = \begin{cases} A \quad \Theta(t)\left(1 - \exp\left(-\frac{(t-t_{init})}{\tau_m}\right)\right)^{h_m} & for\ t > t_0 \\ 0 \qquad otherwise \end{cases} \tag{10}$$

where A is the maximum amplitude, *Θ(t)* is the periodic function made of a composition of cosines described in Fig. S5c; h_m sets the steepness of the function to reach the plateau; t_0 is the time at which muscles get active and τ_m is the time necessary for the function to reach its plateau.

We started to measure the elongation curves immediately before the comma stage, which represents our initial time. We set t_{init}=*90 min*, since around this point of elongation wild type embryos are 1.7-fold long and they start to contract muscles; we also assume that after the 2-fold stage the muscle force has reached its maximum amplitude, which is why we fixed τ_m=*15 min* (the time necessary for a wild type embryo to go from 1.7 to 2 fold; h_m has been arbitrarely set to 1).

The model summarized in Eqs. (5) and (9) has no plateau; however *C. elegans* embryos extend up to 4-fold whithin ≤150 minutes, then stay at this length for ~100 additional minutes before hatching. We do not know why the body length stops at 4-

fold and this issue is not the focus of this work. We can speculate that the ability of the body to remodel is not illimited and may also be restricted by cuticle secretion. In this framework, we can modify Eq.(5) by introducing a multiplicative term under the form of a Hill function to account for the saturation of the elongation:

$$\frac{d\lambda}{dt} = \beta \frac{dl}{dt} \mathrm{H}(\alpha_{DV}) Hill(\lambda) \quad \text{if } \frac{dl}{dt} > 0\ ,\ 0 \leq \beta < 1 \text{ and } l - \lambda > {}^{F_c}/_{k} \quad (11)$$

where $Hill(\lambda) = \frac{L^d}{L^d + \lambda^d}$, with *L* upper threshold for the resting length and *d* an exponent[12]. We set **L=3.2** and **d=15** to account for a rapid saturation of elongation after the 3.2-fold stage, since the wild type embryos show, after this length, a rapid reduction of the elongation rate. By introducing these aditional functions, we can improve the agrement between the data and the model results (Fig. 4j). The Equations presented above have been solved numerically by the Euler method implemented in a Matlab script, with the choice of intitial length $l(0) = \lambda(0) = 1$.

Below is a summary of the parameter values that we fixed on the basis of experimental observations and therefore were not used as free parameters.

Spring	k=1
Dashpot	η=3
F_{epid}	F_{seam}=1, τ_s=50, h_s=4
$F_{muscles}$	τ_m=15 , h_m=1, t_{init}=90
Saturation function	L=3.2, d=15
Critical force F_c	0.5

1.7 Predictiveness of the model. Here we test the model described above by comparing the predicted elongation curves with those observed with another genotype.

When muscle activity was compromised in *spc-1 pak-1* embryos, the retraction phenotype was prevented (Fig. 2). From equations (1) and (7), if $F_{muscles}$ equals zero, then there should be no retraction. Moreover, by fitting the *unc-112*; *spc-1 pak-1* elongation curve we obtained a value of $\alpha_{DV} = 0.64 \pm 0.04$.

1.8 Kelvin-Voigt-type model or Maxwell-type model? In the present work we decided to model the *C. elegans* embryo as a visco-elastic solid with the ability to rearrange its resting length during elongation, and we show that this description can account both for elongation and retraction by changing the behavior of the epidermal force. The Maxwell model[7], as a dashpot and a spring in series, would also account for elongation when the system is under the effect of a positive force. However, a Maxwell-type material keeps extending as soon as a positive force acts on it and this behavior would not account for the muscle-defective *unc-112* embryos. Indeed, these embryos elongate till about 2-fold under the effect of the epidermal force, but does not grow further in the absence of muscle activity, whereas a Maxwell model would predict that its elongation continues.

2- Methods

Animal strains, conditions of maintenance

The list of strains used is presented in Supplementary Table S4. Animals were propagated on NGM agar plates as described previously[13]. Animals were held at a standard 20°C temperature except for experiments implicating *sma-1(ru18); pak-1(tm403)*, in which case L4 animals were shifted to 15°C before egg laying and measures were performed on their offsprings.

Yeast Two Hybrid Screening

Yeast two-hybrid screening was performed by Hybrygenics Services (Paris, France). The bait component was the N-terminal 294 amino acids of PAK-1 (including the regulatory region of the protein) fused as a C-terminal fusion to LexA. The construct was used as a bait to screen at saturation a highly complex, random-primed *C.elegans embryo* cDNA library[14]. Screening involved a mating approach on a medium lacking Trp, Leu and His, supplemented with 0.5 mM 3-aminotriazole[15]. The strongest hits of the screen can be found in Supplementary Table 1. Reciprocal screens using the spectrin repeat #9 or the SH3 domains of SPC-1 as baits identified PAK-1 region 160-206, and no other meaningful prey in the context of the present study.

RNAi enhancer screen and RNAi assays

Two RNAi screens were performed in the *pak-1(tm403)* and in the *spc-1(ra409)* backgrounds along with a wild type control. A collection of 356 essential genes from the Ahringer RNAi library[16], including adhesion proteins, signaling proteins, phosphatases, kinases, cytoskeleton-associated proteins and proteins important in

epithelial morphogenesis, was assembled (Table S1), based on a previous screen performed in the *git-1(tm1962)* background (C. Gally and M. Labouesse, unpublished). The screen was performed in liquid culture on 96-well plates and RNAi knockdown was induced by feeding as described[17]. The primary screen was based on enhanced lethality and body morphology defects; the secondary screen focused on very short larvae and elongation defects. We took DIC images for body length measurements and performed DIC timelapse imaging for the strongest candidates. For specific genes, RNAi was always induced by injection after preparing the double-stranded RNA (dsRNA) with the Ambion mMessage mMachine® kit and purifying the dsRNA with the Qiagen RNeasy® MinElute® Cleanup kit[18]. The embryos were analyzed from 24h to 48h post-injection.

Fluorescent translational reporter constructs

A 12633 bp genomic sequence including the *spc-1* coding sequence and a 3 kb promoter was inserted in frame with the GFP coding sequence present in the pPD95.75 vector (Addgene, Cambridge USA). To create the *Ppak-1::pak-1::mKate* reporter construct, first an mKate-containing backbone was created by exchanging the GFP-coding sequence of the pML1572, P*lin-26::vab-10(ABD)::GFP* plasmid (Gally et al., 2009). In a following cloning step a 8204 bp genomic sequence, including the *pak-1* coding sequence and a 4.5 kb promoter was inserted in frame with the mKate coding sequence present in the vector.

To test if SPC-1::GFP could rescue the function of SPC-1, we first crossed the different transgenic animals of a wild type background with *mnDp33; spc-1(ra409)* animals (strain DM3409), and F1 transgenic males again with DM3409 to establish *mnDp33; spc-1(ra409); Ex[spc-1::GFP]*. Rescuing transgenes were recognized because all

viable progeny was GFP-positive and all (or most) non-viable progeny was GFP-negative, reflecting the loss of the *mnDp33* balancer. To attempt *mnDp33* segregation, we repeatedly transferred single GFP-positive mothers over four generations and examined their progeny, starting from at least two independent extrachromosomal arrays per construct. Thereby, we successfully obtained viable *spc-1(ra409); Ex[Pspc-1::spc-1(+)::gfp]* animals, and then viable *spc-1(ra409) pak-1(tm403); Ex[Pspc-1$_1$::spc-1(+)::gfp]* animals through crossing and meiotic recombination, which segregated very short retracted GFP-negative embryos. For the FHOD-1 constituvely active construct, a 8283 bp genomic sequence of *fhod-1* (gift from David Pruyne[19]) deleted for part of the FH2 domain and the DAD domain was inserted under the control of the epidermis-specific 432 bp *dpy-7* promoter. Deletion of the DAD alone was obtained by inserting back the FH2 domain in the FH2/DAD deleted construct using Hifi DNA assembly cloning kit (New England Biolabs); the FH1/FH2 deleted construct was obtained by deleting the FH1 domain using the Q5 site directed mutagenesis kit protocol (New England Biolabs). All cloning steps relied on the use of the Phusion High-Fidelity DNA Polymerase reaction kit (Fisher Thermo-Scientific); the constructs were subsequently verified by sequencing. The constructs were injected at 10 ng/µl plasmid construct, with 150 ng/µl pBSK + 5 ng/µl pCFJ90 (P$_{myo-2}$*::mcherry*) as co-injection markers for the *spc-1::gfp* constructs, or 100 ng/µl pRF4 (rol) co-injection marker for *pak-1::mKate*.

Fluorescence imaging

DIC images for time-lapse videos were obtained using a Leica DM6000 microscope with a Leica LAS-AF software, using a Leica DMRXA2 upright microscope equipped with a Peltier platform. Observations were done under a 40X oil immersion objective.

Mothers were cut up to gain early-staged embryos, which were then transferred onto thin 5% soft agarose pads in a drop of M9. Z stack image series with a 1,5 µm Z step distance were taken in every 5 minutes during 6 hours. ImageJ software was used to quantify the embryonic length from the end of ventral enclosure/onset of elongation, by taking a "segmented line" through the midline of the embryos from head to tail. To image the coupling between actin bundles displacement in the epidermis and muscle contractions, we used a double reporter strain carrying the epidermal *Pdpy-7::LifeAct::GFP* and muscle *Pmyo-3::his-24::mCherry* transgenes (ML2113, see Table S4), and a spinning-disk DMI6000 Leica microscope equipped with an Andor software (experiments for Fig. 1). Series of five Z planes (1 epidermal + 4 muscle) were imaged continuously for 5 min, with 0,5 µm Z steps and no averaging. The time interval between two Z series was 360 ms. The measurement of actin displacement was done according to the same strategy, and was done using a CSUX1-A1 spinning-disk mounted on a Zeiss Axio Observer Z1 inverted microscope with a Roper Evolve camera controlled by the Metamorph software, and a 100x oil immersion objective (experiments for Fig. S9). A Z-stack of 4 focal planes with 0,5 µm step size was acquired using a streaming acquisition mode. The time between two acquisitions was 0.41 second during 300 time frames. To synchronize embryos, mothers were put on an empty NGM agar plate to lay eggs for a short time window, and embryos were left to develop until the stage of interest. (For the analyse of the contraction see next section on **Image analysis.** To analyse the *in vivo* co-localisation between PAK-1::mKate, ABD::mcherry and SPC-1::GFP, we used the Zeiss/Roper spinning disk microscope under a 100X oil immersion objective, keeping the laser intensity at a constant level throughout the experiments. Image processing and computing the co-localisation coefficient was done using the Volocity software.

Image analysis and quantification of actin filament contraction, continuity and orientation

The analysis of mechanical displacement in the epidermis was performed on the movies of the dorso-ventral actin layer by measuring the distance over time between two landmarks across the region of contraction. The landmarks were set manually on a frame showing relaxed tissue and tracked all over the contraction till the subsequent relaxed state. Landmarks tracking was performed using a statistical template matching approach[20]. The method was implemented as an ImageJ plugin (http://sites.imagej.net/Julienpontabry/), giving as output the landmarks locations, their distance across time and the Kymographs. The curves show a pre-contraction state, a minimum (the maximal contraction point) and an ending part where the distance progressively increases again (see Fig. 1B'' and Fig. S7). After a smoothing and interpolation of the curves, the starting, ending and maximal contraction points were extracted by studying the time derivative of the distance and by setting a threshold on the distance itself. Finally the contraction time was computed as the difference between the ending time and the initial time. The analysis of the curves and statistics were done using a MatLab script. All images were analysed using the ImageJ (FiJi) software (NIH, Bethesda, Maryland, USA; http://rsb.info.nih.gov/ij/) and MATLAB R2014b (The MathWorks Inc., Natick, MA). To study the features of actin pattern, we imaged embryos that were put to sleep by oxygen deprivation through a high concentration of bacteria with the Zeiss/Roper spinning-disk using a 100X oil immersion objective. For each experiments, a Z-stack of 16 focal planes with 0,2 µm step size was acquired. On the original maximum z projection created by imageJ, a manual ROI was defined on the dorso-ventral cells (Fig. 3) from which a high pass filter in the Fourier space was applied to select only structures smaller than 10 pixel of diameter (Fig. 3).

Continuity: The filtered ROIs were binarized by setting to one all the pixels with a value bigger then zero and setting to zero all the other pixels. The resulting structures were then fitted by ellipses from which the length of the Major axis was extracted as a measure of the length of the actin filament. The longer actin filaments are those presenting a more uniform fluorescence along their length (showing higher continuity). By contrast, short segments result from discontinuity in the fluorescence signal. To avoid noise only segments longer than 4 pixels have been considered for the analysis.

Anisotropy of the orientation: The same filtered ROI used for continuity measurements were used to measure the distribution of cable orientation. Fast Fourier Transform (FFT) of these ROIs was computed in order to work in the frequency domain and more easily identify repetitive patterns. The resulting power spectrum of the ROIs was represented in polar coordinates in order to extract the distribution of angles of ROI pattern[21]. The method was implemented in an ImageJ plugin (http://sites.imagej.net/Julienpontabry/), giving as output the angular distribution. In order to compare the distributions coming from different images the distributions were normalized by their integral (Fig. 3). The more the pattern consists in structures oriented in a preferred direction (the more anisotropic), the highest is the peak of the distribution in that direction. In the case of an isotropic pattern, the angular distribution should show a flat behavior. As an estimate of the pattern anisotropy, the prominence of the highest peak of the angular distribution was considered (Fig. 3 and Fig. S4). The analysis of the angular distributions and statistics was performed by a MatLab script. All images were analysed using the ImageJ (FiJi) software (NIH, Bethesda, Maryland, USA; http://rsb.info.nih.gov/ij/) and MATLAB R2014b (The

MathWorks Inc., Natick, MA). All matlab scripts used for the present analysis are available upon request.

Stastical Analysis

For elongation curves, standard deviation was measured. For L1 length measurement and rescue experiments we perform unpaired t-test and ANOVA test using GraphPad Prism 5.00 (San Diego, California, USA) and Excel. For contraction time, actin continuity and orientation, we applied for all genotypes a paired t-test using Matlab.

3-Supplementary figures

Supplementary Figure 1: Local bending of epidermal actin filaments due to muscle contractions

(a-c) Displacement of actin filament marked by LifeAct::GFP at three time points in wild-type embryos. Note their local bending (yellow box). Scale bar, 10 µm.

Supplementary Figure 2: Genes required to maintain embryonic elongation.

(a-g) The proteins GIT-1 and PIX-1 are acting upstream of PAK-1 in the mechano-transduction pathway promoted by muscle contractions, and their loss in the absence of *spc-1* also triggers a retraction phenotype. **(a)** Elongation curves and **(b-g)** terminal phenotypes of **(b)** *pak-1(tm403)*; **(c)** *git-1(tm1962)*; **(d)** *pix-1(gk416)*; **(e)** *spc-1(RNAi) pak-1(tm403)*; **(f)** *git-1(tm1962) spc-1(RNAi)* **(g)** *spc-1(RNAi) pix-1(tm416)*. **(h-k)** The *pak-1(tm403)* mutation also showed synergistic body morphology defects when combined with the null allele *sma-1(ru18)* in the apical ß-spectrin SMA-1, but not as pronounced as for loss of the α-spectrin SPC-1. Quantification of the length at hatching **(h)** and terminal phenotypes of **(i)** *pak-1(tm403)*, **(j)** *sma(ru18)*, **(k)** *sma(ru18); pak-1(tm403)* L1 hatchlings. **(l)** Elongation curves and **(m-n)** terminal phenotypes of **(m)** *unc-112(RNAi)* (n=5) and *unc-112(RNAi); pak-1(tm403)* (n=8) embryos. **(o)** Terminal phenotype of *unc-112(RNAi); spc-1(ra409)* obtained by inducing *unc-112(RNAi)* in the strain ML2436 bearing a rescuing extrachromosomal *spc-1::gfp* array and looking for embryos having lost the array; due to high stability of the array few embryos were obtained despite numerous repeats (n=4), which all had the phenotype illustrated here and is similar to that of *spc-1(ra409)* alone. Scale bars: 17 µm **(b-g; m-o)**; 50 µm **(i- k)**.

Supplementary Figure 3: PAK-1and SPC-1 colocalized with actin filaments

(a) Distribution of PAK-1::mKate in a late embryo (n=20). Enlarged pictures of PAK-1 showing a filamentous distribution in the dorso-ventral epidermis similar to actin filaments. Scale bar: 25 µm. **(b)** Fuorescence pictures of PAK-1::mKate (red) and SPC-1::GFP (green): the panel shows the colocalization image for the most apical focal planes (top image), and full XZ (green panel) and YZ (red panel) projections. The level of co-localization is high based on Pearson's correlation coefficient (0.7-0.9, n=20). The highest level of co-localization is detected at the apical cortex**. (c)** Fuorescence pictures of *Plin-26*::VAB-10(ABD)::mCherry (red) and SPC-1::GFP (green): the panel shows the colocalization image for the most apical focal planes (top image), and full XZ (green panel) and YZ (red panel) projections. The level of co-localization is high based on Pearson's correlation coefficient (0.7-0.9, n=8). The co-localization is almost exclusively detected at the apical cortex. The gene *lin-26* drives expression in the epidermis; VAB-10(ABD) corresponds to the two actin-binding domains (calponin homology) of the protein VAB-10. Scale bar, 10 µm.

Supplementary Figure 4: Actin filament continuity and orientation at three elongation stages

Actin filaments were visualised using a *Pepid::Lifeact::GFP* construct and characterised as outlined in Fig. 3a (the *Pepid* promoter corresponds to *Pdpy-7*). **(a)** Actin filament continuity. The graph represents the length (in pixels) along the circumferential axis of actin filaments in early, mid and late (corresponding to 1.7-fold, 2-fold and 3-fold equivalent stages in a wild-type embryo, respectively) embryos of wild-type (early n=12, mid n=19, late n=16), *pak-1(tm403)* (early n=16, mid n=21, late n=16), *spc-1(RNAi)* (early n=15, mid n=21, late n=20), and *spc-1(RNAi) pak-1(tm403)* (early n=12, mid n=17, late n=26) genotypes. **(b)** Actin filament orientation

based on Fast Fourier Transform and binarisation. Wild type (early n=12, mid n=18, late n=14), *pak-1(tm403)* (early n=16, mid n=20, late n=16), *spc-1(RNAi*(early n=14, mid n=18, late n=18), and *pak-1(tm403) + spc-1(RNAi)* (early n=12, mid n=18, late n=21). Note that the characteritics of actin filaments in *spc-1(RNAi) pak-1(tm403)* embryos differ mostly at the equivalent of the two-fold stage when muscles become active. At ealier and later stages, *spc-1(RNAi)* embryos and *spc-1(RNAi) pak-1(tm403)* embryos become similar. **(c-f)** Epidermal actin filaments visualized with the Pepid::Lifeact::GFP construct in wild-type (C), *spc-1(RNAi) pak-1(tm403)* (D) embryos (panels are from Fig. 3). *<0,05; **<0,001; ***<0,0001; ns, not significant.

Supplementary Figure 5: Change in embryo diameter during elongation

(a-b'') Fluorescence micrographs of embryos expressing the *Pepid*::*Lifeact*::*GFP* construct in the epidermis at three elongation stages early, middle and late (corresponding to 1.7-fold, 2-fold and 3-fold equivalent stages in a wild-type embryo, respectively) for wild-type **(a-a'')** and *spc-1(RNAi) pak-1(tm403)* embryos **(b-b'')**; the *Pepid* promoter corresponds to *Pdpy-7***.** The yellow lines correspond to the segments used to measure the dorso-ventral width of the V1 seam cell. (**c)** Quantification of the average V1 cell width normalized to the initial width during elongation in four genotypes. **(d)** Quantification of the average dorso-ventral width at the level of the V1 seam cell, which was calculated using the measured embryo length and V1 cell width, taking into consideration the conservation of the total embryo volume. Each point in panel **(c)** and **(d)** represents between 7 and 21 embryos; error bars are standard errors. A notable feature of *spc-1(RNAi) pak-1(tm403)* embryos is that the circumferential dimension of the seam cells decreased much more than that of their DV cell, which most likely reflects the actin filament integrity defects combined with a F_{seam} force largely unchanged.

Supplementary Figure 6: Time-dependent length of a Kelvin-Voigt model in different conditions.

(a-a') A generic Kelvin-Voigt system subject to a constant force F_{epid} and its predicted elongation change using F_{epid}=0.85 (A'). **(b-b')** A similar system subject to two forces, F_{epid} and an oscillating force $F_{muscles}$ with the properties depicted in (E), and predicted elongation change using F_{epid}=0.85 (B'). As the pulsatile force induces both compression and stretching (see Fig. S6), its net input on elongation is transient and the system oscillates around the maximal value reached without $F_{muscles}$. **(d-d')** A Kelvin-Voigt system with mechanichal plasticity introduced according to Eqs. (1,4-7), and predicted elongation change using F_{epid}=0.85, β=0.10 and F_c=0 according to Eqs. (1,4-7). **(e)** A Kelvin-Voigt system in which the plasticity is defective (β=0), and there is actin tearing according to Eq. (7) inducing a progressive reduction of F_{epid}, and predicted elongation change using F_{epid}=0.85, with an initial value of the passive component $\alpha_{DV}(t=0)=1$ and the tearing factor γ=0.15 (D'). **(e' Inset)** Behavior of $\alpha_{DV}(t)$. **(c)** In all conditions $F_{muscles}$ is a periodic function with positive and negative steps of duration of 6 seconds alternating with periods of null value of duration 15 seconds modulated by a cosine function. In **(a-e')** the elastic constant of the spring is k=1, the initial resting length has the value $\lambda(t=0)=1$, and the viscosity value is η=10. **(f)** Result of the fit for the following genotypes: *wt*, *spc-1 pak-1*, *unc-112* and *spc-1* according to Eqs. (1,4-7). The values of the parameters are specified in paragraphs 1.4, 1.5 and 1.6.

Supplementary Figure 7: Comparable retraction phenotypes after the combined loss of SPC-1 and PAK-1 or SPC-1 and FHOD-1

(a) Elongation curves of the single and double deficient embryos indicated on the left, **(b-h)** and corresponding terminal phenotypes at hatching: wild-type (n=5), *fhod-1(tm2363)* (n=6) *fhod-1(RNAi)* (n=7) *pak-1(tm403)* (n=5) *fhod-1(RNAi); pak1(tm403)* (n=7), *spc-1(RNAi) pak-1(tm403)* (n=8), *fhod-1(tm2363);spc-1(RNAi)* (n=9). Scale bar, 25 µm.

Supplementary Figure 8: PAK-1 and FHOD-1 form aggregates in *spc-1(RNAi)* loss of function.

(a-a') PAK-1::GFP localisation in wild-type and *spc-1(RNAi)* embryos. Yellow box, area enlarged below the panel. Note the punctae in SPC-1 deficient embryos. (**b-b'**) FHOD-1 localization in wild-type and *spc-1(RNAi)* embryos. Note the aggregates (arrowheads). Note also that FHOD-1::GFP displayed a filamentous organization reminiscent of actin filaments. Scale bar: 10 µm.

Supplementary Figure 9: Actin displacement ratio

(a-d) Individual displacement tracks of actin filaments visualized with a *Pdpy-7::Lifeact::GFP* marker specifically expressed in the epidermis of wild type **(a),** *pak-1(tm403)* **(b),** *spc-1(RNAi)* **(c)** and *spc-1(RNAi) pak-1(tm403)* **(d)** embryos at a stage equivalent to 2-fold in a wild-type embryo. Scale bar: 10 µm. **(e)** Typical kymographs of *Pepid::Lifeact::GFP*–labeled actin filaments in wild-type and *spc-1(RNAi) pak-1(tm403)* embryos from which the tracks in a-d were derived. Yellow dots correspond to landmarks for quantitative analysis. **(f)** Quantification of the displacement duration in (N=embryo/ n=contraction): wild-type, N=11/n=51; *pak-1(tm403)*, N=11/n=26; *spc-1(RNAi)*, N=11/n=73; *spc-1(RNAi) pak-1(tm403)*, N=11/n=89. *<0,05; **<0,001; ***<0,0001; ns, not significant.

4-Caption for movies

Movie 1: Combined DIC timelapse movie. Image acquisition was every 5 minutes in wild-type, *pak-1(tm403)*, *spc-1(RNAi)*, *spc-1(RNAi) pak-1(tm403) embryos*. Scale Bar, 10 µm.

Movie 2: Combined DIC timelapse movie of *unc-112(RNAi)* and *unc 112(RNAi); spc-1(RNAi) pak-1(tm403)* embryos. Scale Bar,10 µm.

Movie 3: Combined DIC timelapse movies of *spc-1(ra409)* and *fhod-1(RNAi); spc-1(ra409)* embryos. Scale Bar, 10 µm.

Movie 4: Fluorescence movie showing the displacement of actin filaments labelled with *Pdpy-7::lifeact::GFP* in the epidermis. Time acquisition is 0.41 s in wild-type, *pak-1(tm403)*, *spc-1(RNAi)* and *spc-1(RNAi) pak-1(tm403)* embryos. Scale Bar,10 µm.

5-Supplementary references

1 Vuong-Brender, T. T., Yang, X. & Labouesse, M. C. elegans Embryonic Morphogenesis. *Curr Top Dev Biol* **116**, 597-616, doi:10.1016/bs.ctdb.2015.11.012 (2016).

2 Vuong-Brender, T. T., Ben Amar, M., Pontabry, J. & Labouesse, M. The interplay of stiffness and force anisotropies drive embryo elongation. *Elife* **6**, doi:10.7554/eLife.23866 (2017).

3 Rauzi, M., Lenne, P. F. & Lecuit, T. Planar polarized actomyosin contractile flows control epithelial junction remodelling. *Nature* **468**, 1110-1114, doi:nature09566 [pii]
10.1038/nature09566 (2010).

4 Diogon, M. *et al.* The RhoGAP RGA-2 and LET-502/ROCK achieve a balance of actomyosin-dependent forces in C. elegans epidermis to control morphogenesis. *Development* **134**, 2469-2479, doi:dev.005074 [pii]

10.1242/dev.005074 (2007).
5 Williams, B. D. & Waterston, R. H. Genes critical for muscle development and function in *Caenorhabditis elegans* identified through lethal mutations. *J Cell Biol* **124**, 475-490. (1994).
6 Vincent, J. in *Structural Biomaterials: Third Edition* 1-28 (Princeton University Press, 2012).
7 Meyers, M. A. & Chawla, K. K. *Mechanical Behavior of Materials*. (Cambridge University Press, 2008).
8 Doubrovinski, K., Swan, M., Polyakov, O. & Wieschaus, E. F. Measurement of cortical elasticity in Drosophila melanogaster embryos using ferrofluids. *Proc Natl Acad Sci U S A* **114**, 1051-1056, doi:10.1073/pnas.1616659114 (2017).
9 Munoz, J. J. & Albo, S. Physiology-based model of cell viscoelasticity. *Phys Rev E Stat Nonlin Soft Matter Phys* **88**, 012708, doi:10.1103/PhysRevE.88.012708 (2013).
10 Norman, K. R. & Moerman, D. G. Alpha spectrin is essential for morphogenesis and body wall muscle formation in Caenorhabditis elegans. *The Journal of cell biology* **157**, 665-677, doi:10.1083/jcb.200111051 (2002).
11 Hansen, N. & Ostermeier, A. Completely derandomized self-adaptation in evolution strategies. *Evol Comput* **9**, 159-195, doi:10.1162/106365601750190398 (2001).
12 Alon, U. (Chapman & Hall/CRC, Boca Raton, 2007).
13 Brenner, S. The genetics of Caenorhabditis elegans. *Genetics* **77**, 71-94 (1974).
14 Gomes, J. E. *et al.* Microtubule severing by the katanin complex is activated by PPFR-1-dependent MEI-1 dephosphorylation. *J Cell Biol* **202**, 431-439, doi:10.1083/jcb.201304174 (2013).
15 Fromont-Racine, M., Rain, J. C. & Legrain, P. Toward a functional analysis of the yeast genome through exhaustive two-hybrid screens. *Nat Genet* **16**, 277-282, doi:10.1038/ng0797-277 (1997).
16 Kamath, R. S. *et al.* Systematic functional analysis of the *Caenorhabditis elegans* genome using RNAi. *Nature* **421**, 231-237 (2003).
17 Gally, C., Zhang, H. & Labouesse, M. Functional and Genetic Analysis of VAB-10 Spectraplakin in *Caenorhabditis elegans*. *Methods in Enzymology* **in press**, doi:http://dx.doi.org/10.1016/bs.mie.2015.05.005 (2015).
18 Bosher, J. M. *et al.* The *Caenorhabditis elegans vab-10* spectraplakin isoforms protect the epidermis against internal and external forces. *J Cell Biol* **161**, 757-768 (2003).
19 Mi-Mi, L., Votra, S., Kemphues, K., Bretscher, A. & Pruyne, D. Z-line formins promote contractile lattice growth and maintenance in striated muscles of C. elegans. *J Cell Biol* **198**, 87-102, doi:10.1083/jcb.201202053 (2012).
20 Matthews, I., Ishikawa, T. & Baker, S. The template update problem. *IEEE Trans Pattern Anal Mach Intell* **26**, 810-815, doi:10.1109/TPAMI.2004.16 (2004).
21 Gonzalez, R. C. & Woods, R. E. *Digital Image Processing (3rd Edition)*. (Prentice-Hall, Inc, 2006).

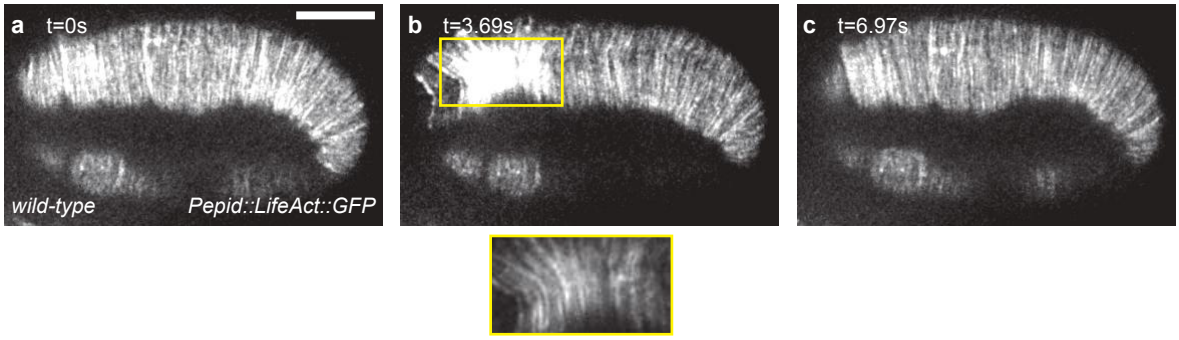

Supplementary Figure 1: Local bending of epidermal actin filaments due to muscle contractions

(a-c) Displacement of actin filament marked by LifeAct::GFP at three time points in wild-type embryos. Note their local bending (yellow box). Scale bar, 10 µm.

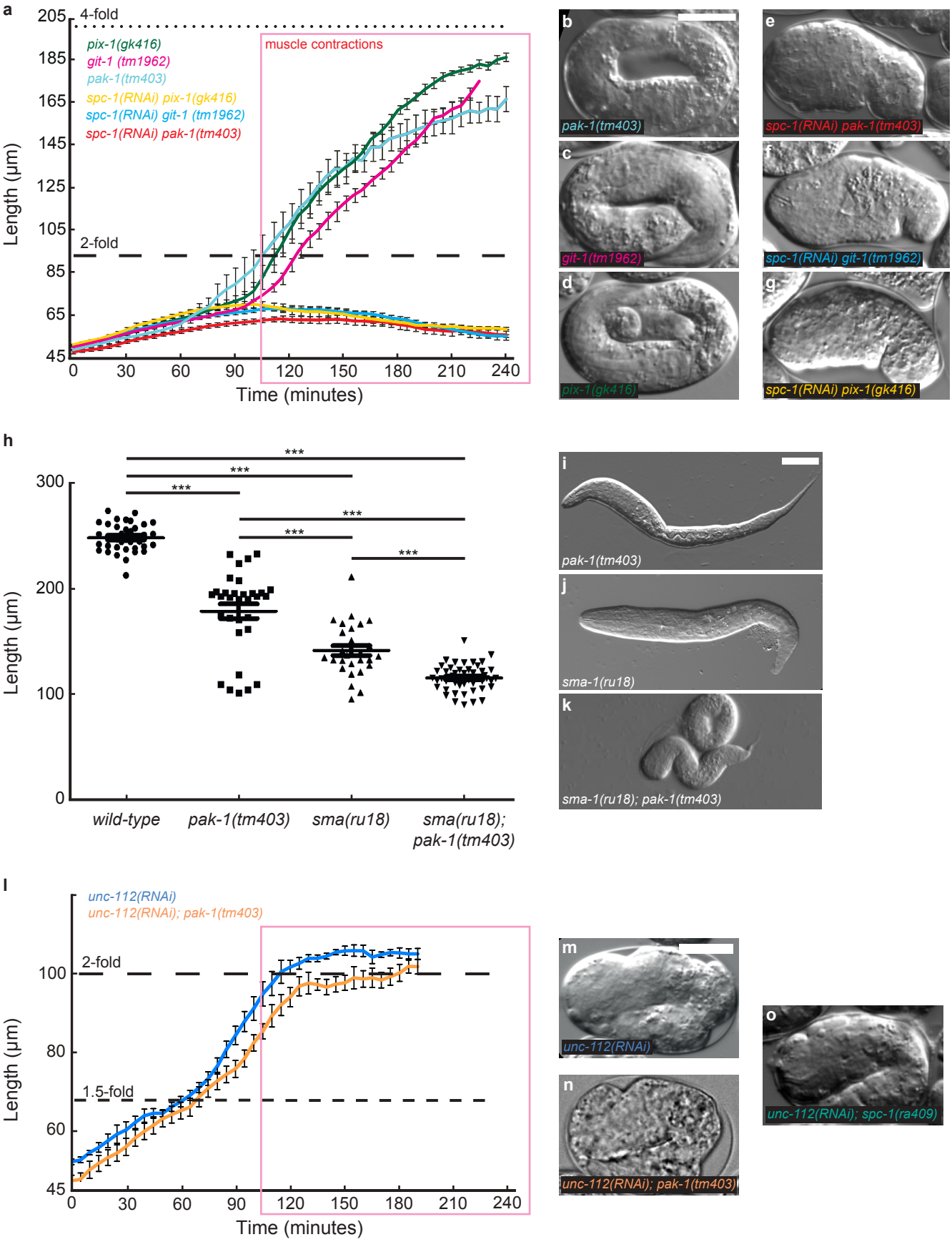

Supplementary Figure 2: Genes required to maintain embryonic elongation.

(a-g) The proteins GIT-1 and PIX-1 are acting upstream of PAK-1 in the mechano-transduction pathway promoted by muscle contractions, and their loss in the absence of spc-1 also triggers a retraction phenotype.
(a) Elongation curves and (b-g) terminal phenotypes of (b) pak-1(tm403); (c) git-1(tm1962); (d) pix-1(gk416); (e) spc-1(RNAi) pak-1(tm403); (f) git-1(tm1962) spc-1(RNAi) (g) spc-1(RNAi) pix-1(tm416).
(h-k) The pak-1(tm403) mutation also showed synergistic body morphology defects when combined with the null allele sma-1(ru18) in the apical ß-spectrin SMA-1, but not as pronounced as for loss of the α-spectrin SPC-1. Quantification of the length at hatching (h) and terminal phenotypes of (i) pak-1(tm403), (j) sma(ru18), (k) sma(ru18); pak-1(tm403) L1 hatchlings.
(l) Elongation curves and (m-n) terminal phenotypes of (m) unc-112(RNAi) (n=5) and unc-112(RNAi); pak-1(tm403) (n=8) embryos.
(o) Terminal phenotype of unc-112(RNAi); spc-1(ra409) obtained by inducing unc-112(RNAi) in the strain ML2436 bearing a rescuing extrachromosomal spc-1::gfp array and looking for embryos having lost the array; due to high stability of the array few embryos were obtained despite numerous repeats (n=4), which all had the phenotype illustrated here and is similar to that of spc-1(ra409) alone. Scale bars: 17 µm (b-g; m-o); 50 µm (i- k).

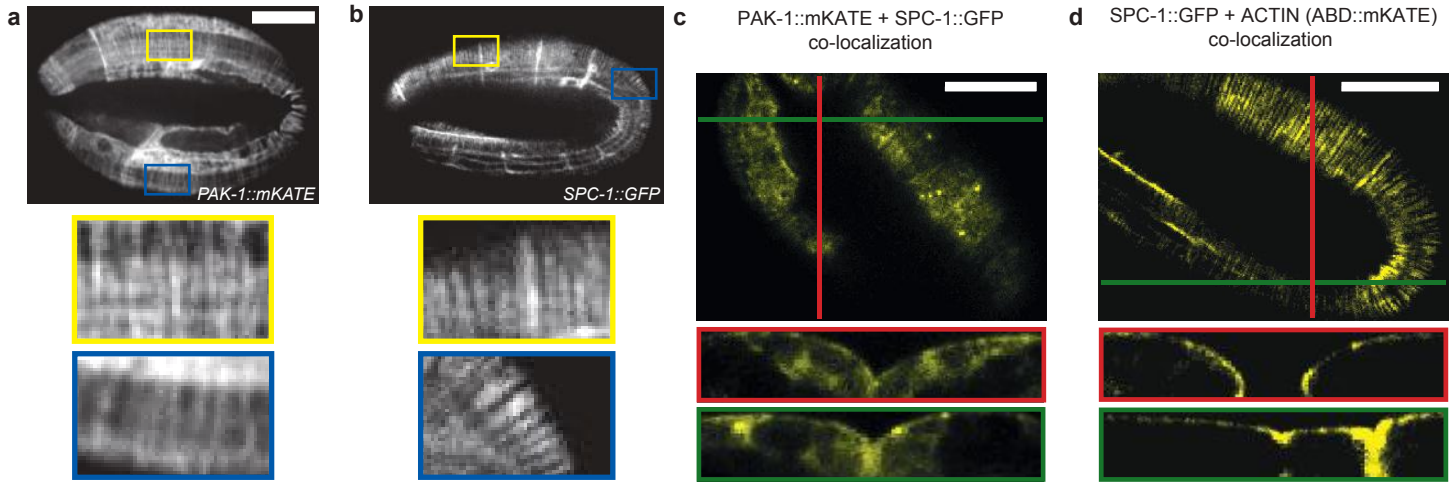

Supplementary Figure 3: PAK-1and SPC-1 colocalized with actin filaments

(a) Distribution of PAK-1::mKate in a late embryo (n=20). Enlarged pictures of PAK-1 showing a filamentous distribution in the dorso-ventral epidermis similar to actin filaments. Scale bar: 25 µm.
(b) Fuorescence pictures of PAK-1::mKate (red) and SPC-1::GFP (green):
the panel shows the colocalization image for the most apical focal planes (top image), and full XZ (green panel) and YZ (red panel) projections. The level of co-localization is high based on Pearson's correlation coefficient (0.7-0.9, n=20). The highest level of co-localization is detected at the apical cortex.
(c) Fuorescence pictures of Plin-26::VAB-10(ABD)::mCherry (red) and SPC-1::GFP (green): the panel shows the colocalization image for the most apical focal planes (top image), and full XZ (green panel) and YZ (red panel) projections. The level of co-localization is high based on Pearson's correlation coefficient (0.7-0.9, n=8). The co-localization is almost exclusively detected at the apical cortex.
The gene lin-26 drives expression in the epidermis; VAB-10(ABD) corresponds to the two actin-binding domains (calponin homology) of the protein VAB-10. Scale bar, 10 µm.

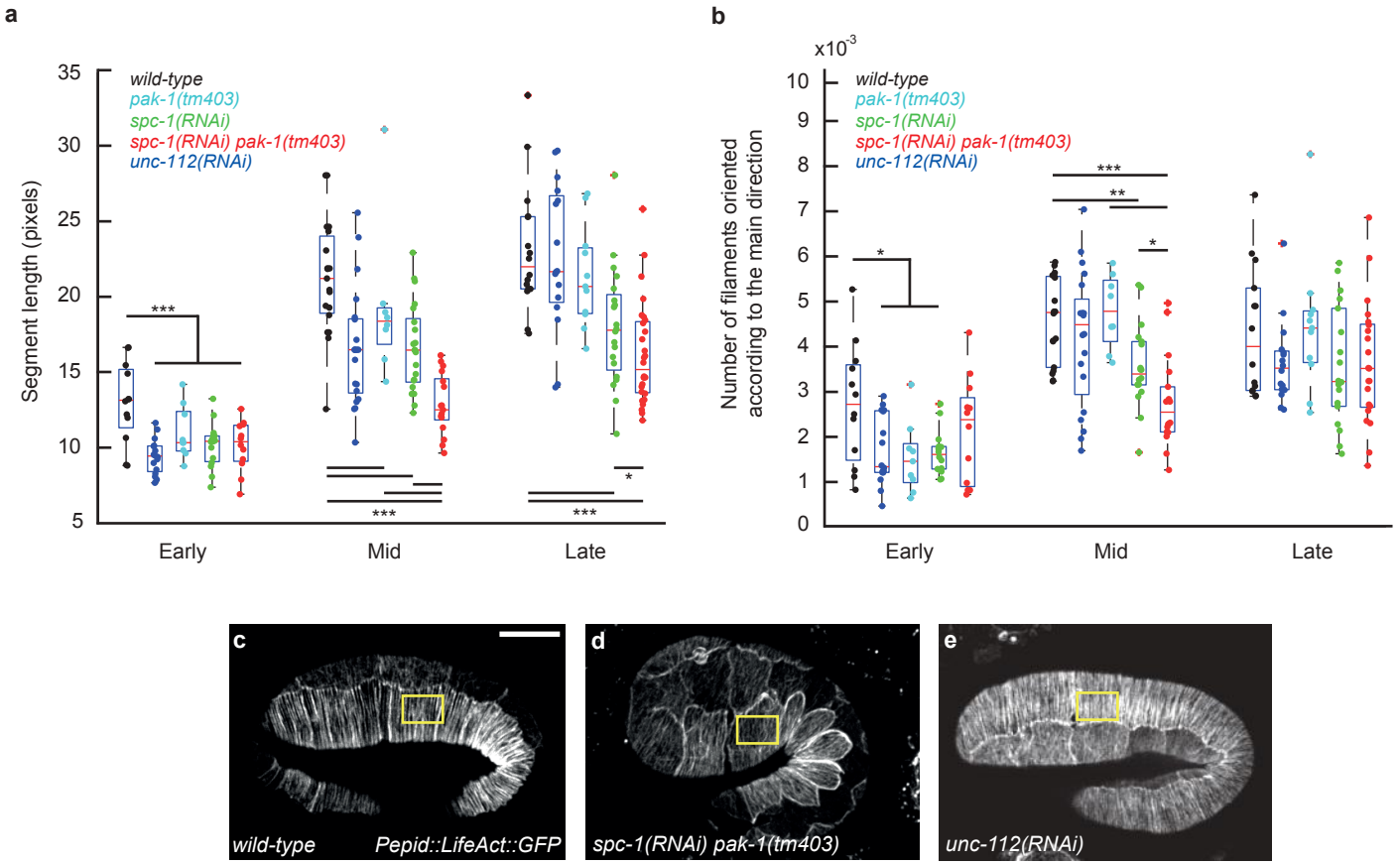

Supplementary Figure 4: Actin filament continuity and orientation at three elongation stages

Actin filaments were visualised using a Pepid::Lifeact::GFP construct and characterised as outlined in Fig. 3a
(the Pepid promoter corresponds to Pdpy-7).
(a) Actin filament continuity. The graph represents the length (in pixels) along the circumferential axis of actin filaments in early, mid and late (corresponding to 1.7-fold, 2-fold and 3-fold equivalent stages in a wild-type embryo, respectively) embryos of wild-type (early n=12, mid n=19, late n=16), pak-1(tm403) (early n=16, mid n=21, late n=16), spc-1(RNAi) (early n=15, mid n=21, late n=20), and spc-1(RNAi) pak-1(tm403) (early n=12, mid n=17, late n=26) genotypes.
(b) Actin filament orientation based on Fast Fourier Transform and binarisation. Wild type (early n=12, mid n=18, late n=14), pak-1(tm403) (early n=16, mid n=20, late n=16), spc-1(RNAi(early n=14, mid n=18, late n=18), and pak-1(tm403) + spc-1(RNAi) (early n=12, mid n=18, late n=21).
Note that the characteritics of actin filaments in spc-1(RNAi) pak-1(tm403) embryos differ mostly at the equivalent of the two-fold stage when muscles become active. At ealier and later stages, spc-1(RNAi) embryos and spc-1(RNAi) pak-1(tm403) embryos become similar.
(c-f) Epidermal actin filaments visualized with the Pepid::Lifeact::GFP construct in wild-type (C), spc-1(RNAi) pak-1(tm403) (D) embryos (panels are from Fig. 3). *<0,05; **<0,001; ***<0,0001; ns, not significant.

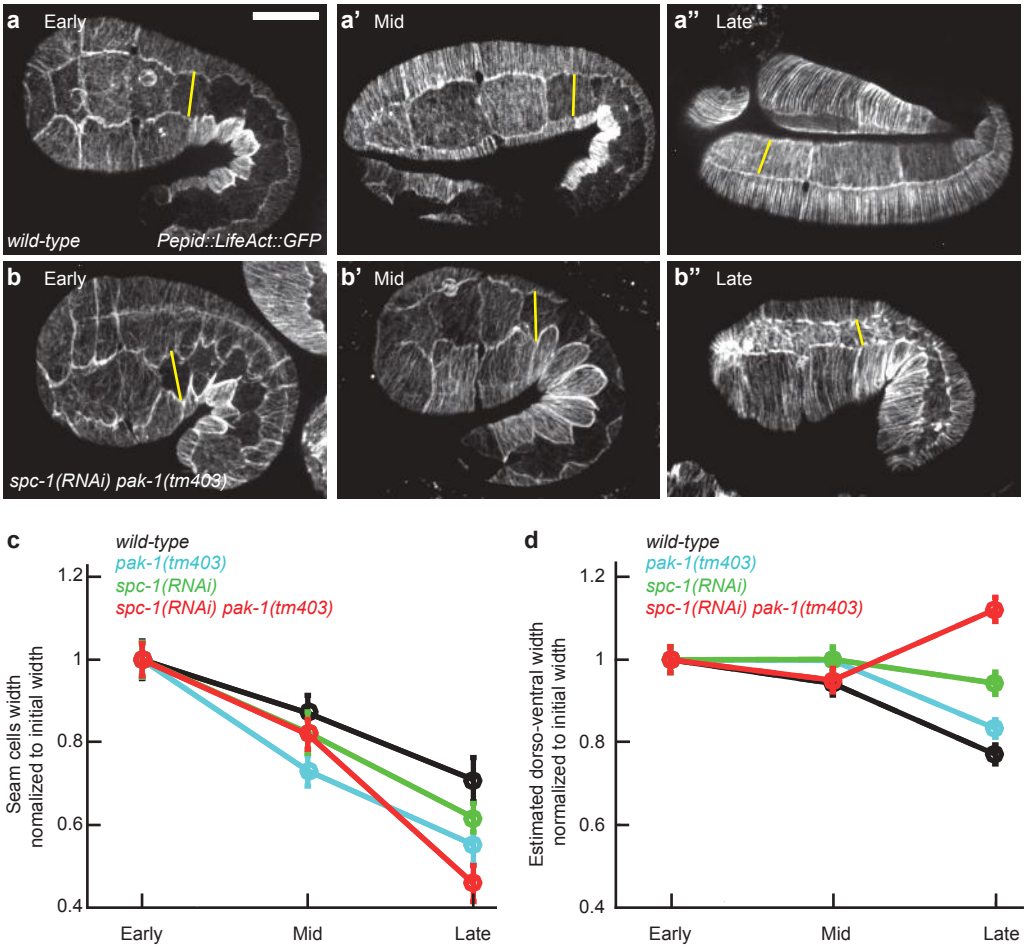

Supplementary Figure 5: Change in embryo diameter during elongation

(a-b'') Fluorescence micrographs of embryos expressing the Pepid::Lifeact::GFP construct in the epidermis at three elongation stages early, middle and late (corresponding to 1.7-fold, 2-fold and 3-fold equivalent stages in a wild-type embryo, respectively) for wild-type (a-a'') and spc-1(RNAi) pak-1(tm403) embryos (b-b''); the Pepid promoter corresponds to Pdpy-7. The yellow lines correspond to the segments used to measure the dorso-ventral width of the V1 seam cell. (c) Quantification of the average V1 cell width normalized to the initial width during elongation in four genotypes. (d) Quantification of the average dorso-ventral width at the level of the V1 seam cell, which was calculated using the measured embryo length and V1 cell width, taking into consideration the conservation of the total embryo volume. Each point in panel (c) and (d) represents between 7 and 21 embryos; error bars are standard errors.
A notable feature of spc-1(RNAi) pak-1(tm403) embryos is that the circumferential dimension of the seam cells decreased much more than that of their DV cell, which most likely reflects the actin filament integrity defects combined with a Fseam force largely unchanged.

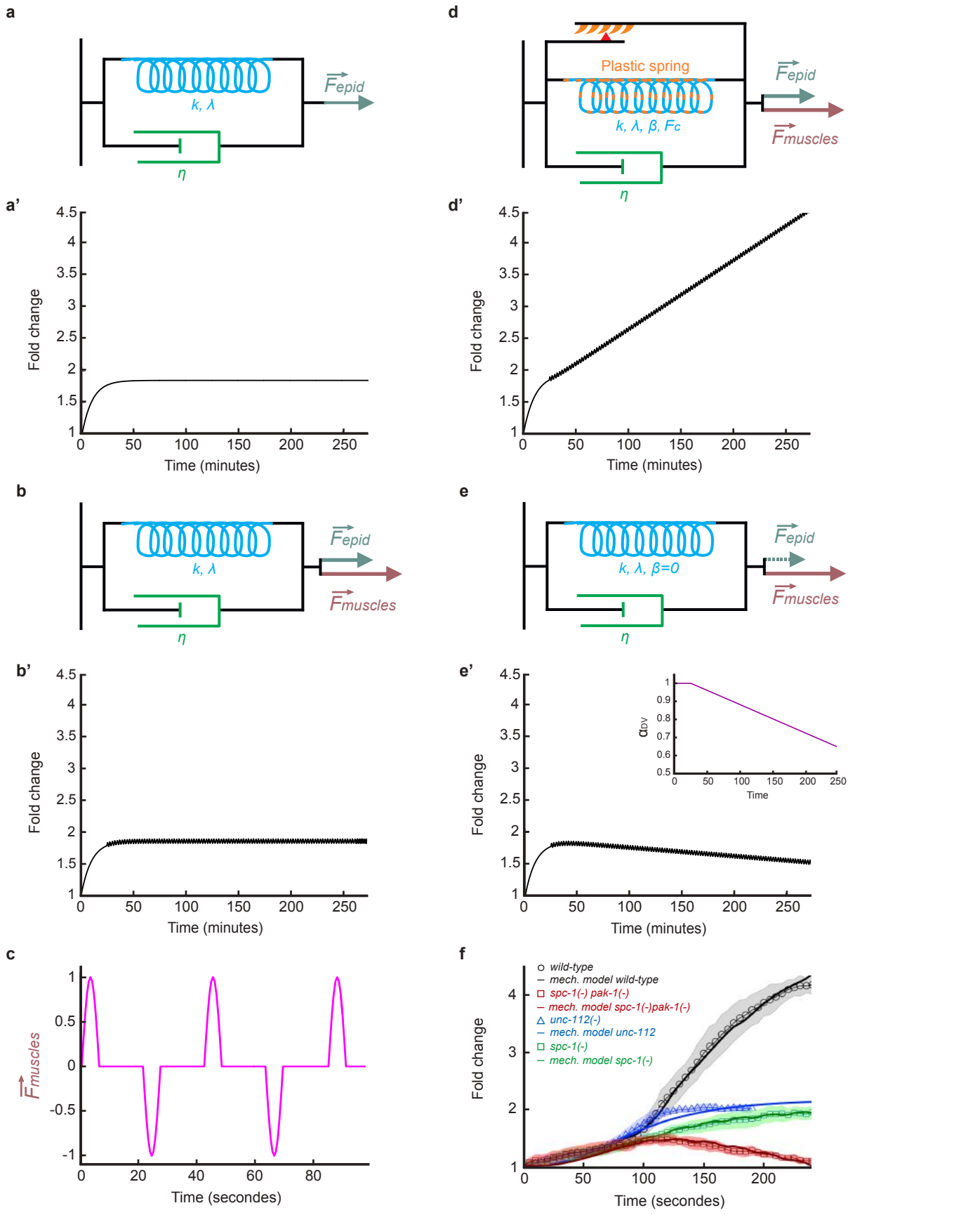

Supplementary Figure 6: Time-dependent length of a Kelvin-Voigt model in different conditions.

(a-a') A generic Kelvin-Voigt system subject to a constant force Fepid and its predicted elongation change using Fepid=0.85 (A').
(b-b') A similar system subject to two forces, Fepid and an oscillating force Fmuscles with the properties depicted in (E), and predicted elongation change using Fepid=0.85 (B'). As the pulsatile force induces both compression and stretching (see Fig. S6), its net input on elongation is transient and the system oscillates around the maximal value reached without Fmuscles.
(d-d') A Kelvin-Voigt system with mechanichal plasticity introduced according to Eqs. (1,4-7), and predicted elongation change using Fepid=0.85, β=0.10 and Fc=0 according to Eqs. (1,4-7). (e) A Kelvin-Voigt system in which the plasticity is defective (β=0), and there is actin tearing according to Eq. (7) inducing a progressive reduction of Fepid, and predicted elongation change using Fepid=0.85, with an initial value of the passive component αDV(t=0)=1 and the tearing factor γ=0.15 (D').
(e' Inset) Behavior of αDV(t).
(c) In all conditions Fmuscles is a periodic function with positive and negative steps of duration of 6 seconds alternating with periods of null value of duration 15 seconds modulated by a cosine function. In (a-e') the elastic constant of the spring is k=1, the initial resting length has the value λ(t=0)=1, and the viscosity value is η=10. (f) Result of the fit for the following genotypes: wt, spc-1 pak-1, unc-112 and spc-1 according to Eqs. (1,4-7). The values of the parameters are specified in paragraphs 1.4, 1.5 and 1.6.

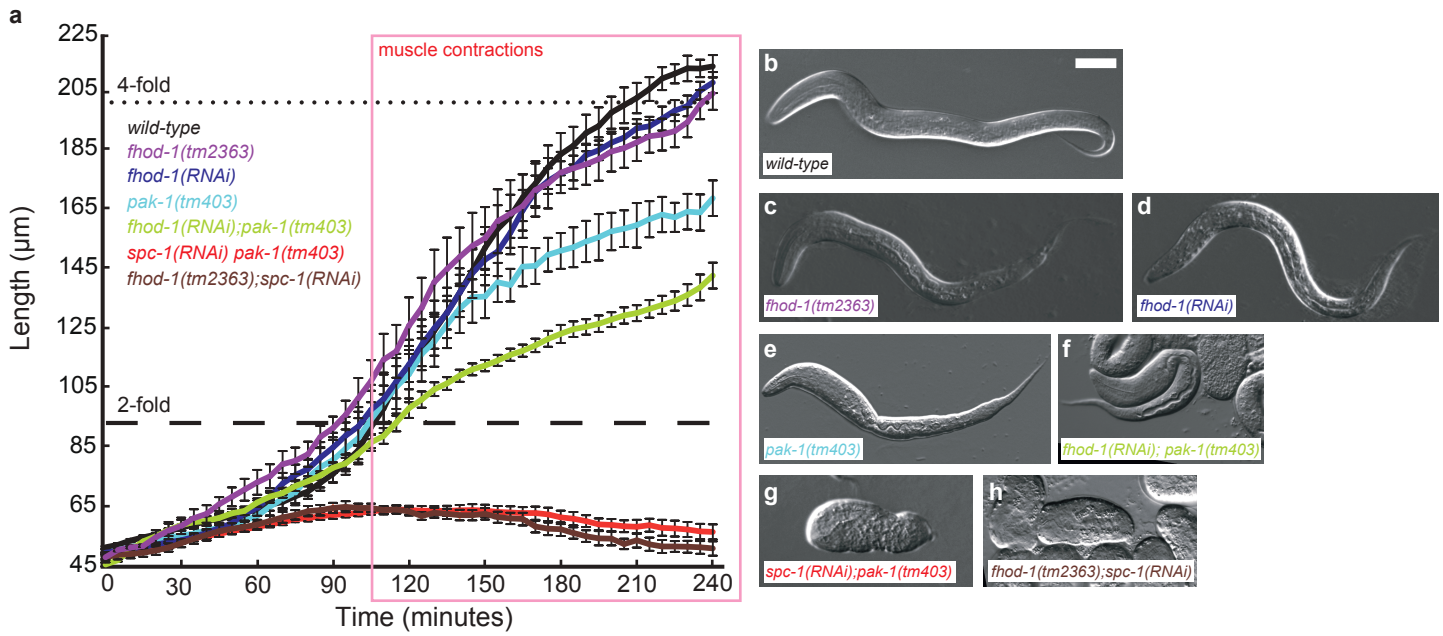

Supplementary Figure 7: Comparable retraction phenotypes after the combined loss of SPC-1 and PAK-1 or SPC-1 and FHOD-1

(a) Elongation curves of the single and double deficient embryos indicated on the left,
(b-h) and corresponding terminal phenotypes at hatching: wild-type (n=5), fhod-1(tm2363) (n=6) fhod-1(RNAi) (n=7) pak-1(tm403) (n=5) fhod-1(RNAi); pak1(tm403) (n=7), spc-1(RNAi) pak-1(tm403) (n=8), fhod-1(tm2363);spc-1(RNAi) (n=9). Scale bar, 25 µm.

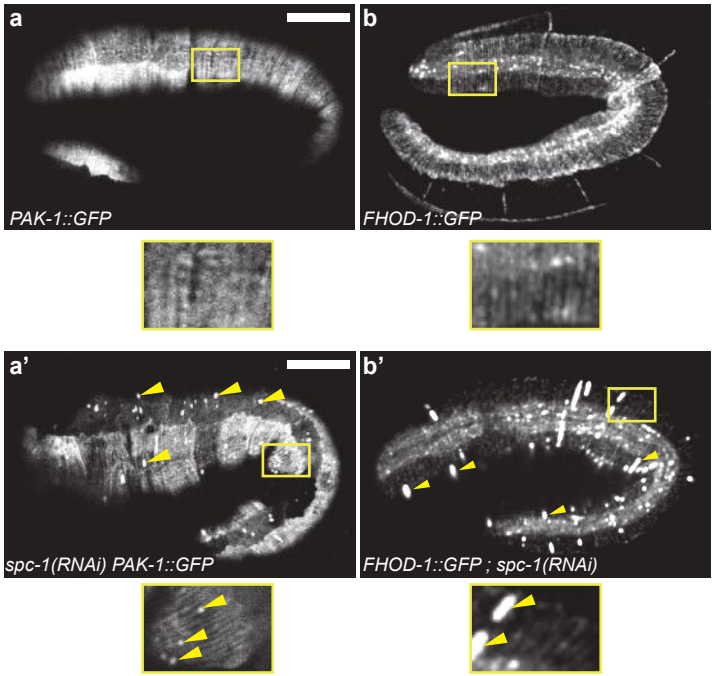

Supplementary Figure 8: PAK-1 and FHOD-1 form aggregates in spc-1(RNAi) loss of function.

(a-a') PAK-1::GFP localisation in wild-type and spc-1(RNAi) embryos. Yellow box, area enlarged below the panel.
Note the punctae in SPC-1 deficient embryos.
(b-b') FHOD-1 localization in wild-type and spc-1(RNAi) embryos.
Note the aggregates (arrowheads). Note also that FHOD-1::GFP displayed a filamentous organization reminiscent of actin filaments.
Scale bar: 10 µm.

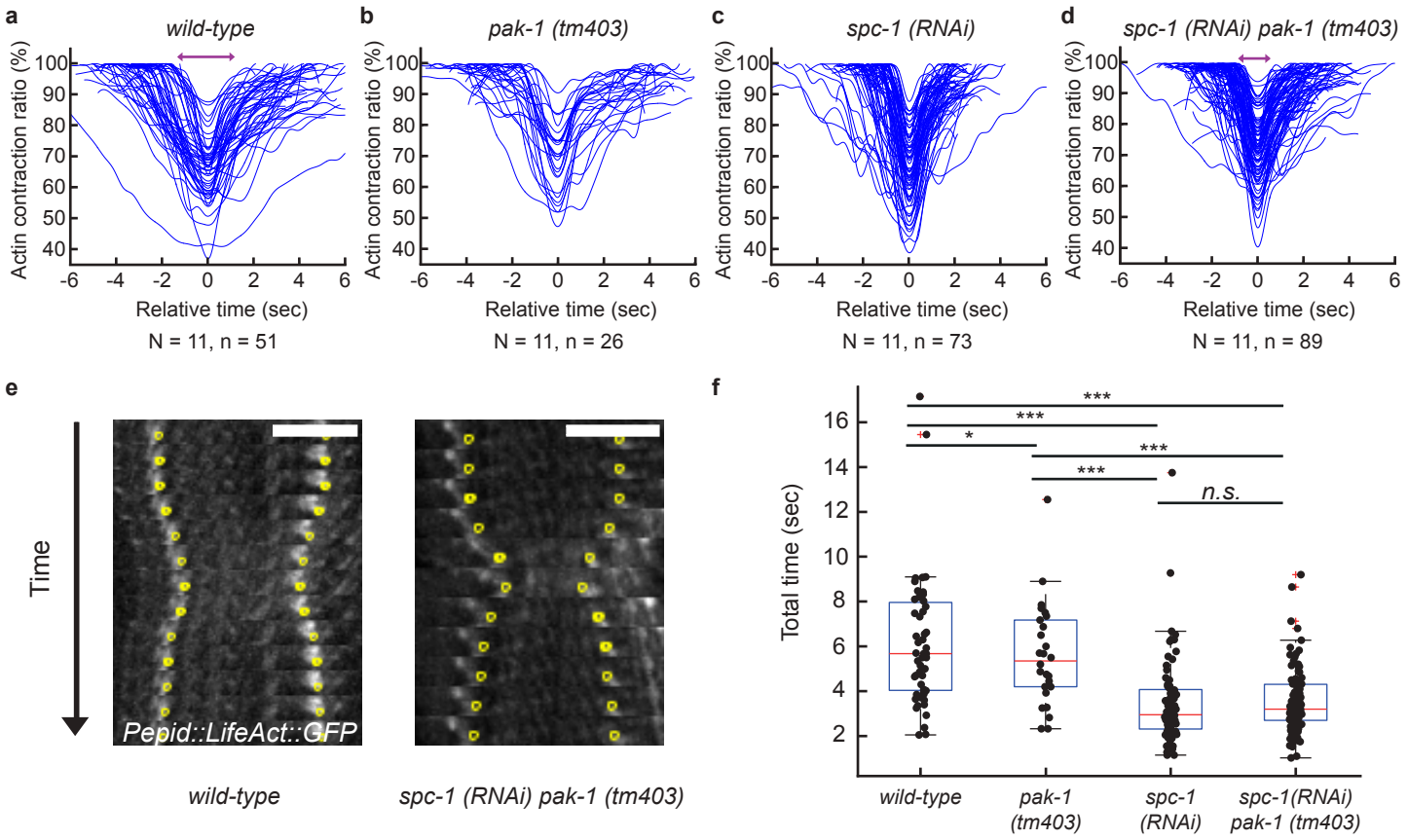

Supplementary Figure 9: Actin displacement ratio

(a-d) Individual displacement tracks of actin filaments visualized with a Pdpy-7::Lifeact::GFP marker specifically expressed in the epidermis of wild type (a), pak-1(tm403) (b), spc-1(RNAi) (c) and spc-1(RNAi) pak-1(tm403) (d) embryos at a stage equivalent to 2-fold in a wild-type embryo. Scale bar: 10 µm.
(e) Typical kymographs of Pepid::Lifeact::GFP–labeled actin filaments in wild-type and spc-1(RNAi) pak-1(tm403) embryos from which the tracks in a-d were derived. Yellow dots correspond to landmarks for quantitative analysis.
(f) Quantification of the displacement duration in (N=embryo/ n=contraction): wild-type, N=11/n=51; pak-1(tm403), N=11/n=26; spc-1(RNAi), N=11/n=73; spc-1(RNAi) pak-1(tm403), N=11/n=89. *<0,05; **<0,001; ***<0,0001; ns, not significant.

A	Reproducible 50-100% enhanced defect* compared to wild-type
B	Reproducible 20-50% enhanced defect* compared to wild-type
C	Reproducible 5-20% enhanced defect* compared to wild-type

Targeted gene	***Function***	***Strength of interaction***
(III) ani-1	**Anilin**	**A**
(IV) cap-1	**F-actin capping protein α subunit**	**A**
(II) cap-2	**β subunit of actin capping protein**	**A**
(V) cdc-25.2	**Putative homolog of Cdc25 phosphatase**	**A**
(II) cdc-42	**RHO GTPase**	**A**
(III) dlc-1	**Dynein light chain**	**A**
(IV) epi-1	**Laminin α chain**	**A**
(I) hmp-2	**β-catenin**	**A**
(IV) lam-1	**Laminin β**	**A**
(I) let-502	**Rho-binding Ser/Thr kinase**	**A**
(III) mlc-5	**Myosin II essential light chain ortholog**	**A**
(I) pfn-1	**Profilin**	**A**
(V) sma-1	**βH-spectrin**	**A**
(X) spc-1	**α-spectrin**	**A**
(I) sur-6	**Regulatory subunit of serine/threonine protein phosphatase 2A**	**A**
(X) tni-1	**Troponin**	**A**
(II) dsh-2	**Dishevelled (Dsh) homolog**	**B**
(I) goa-1	**Ortholog of the heterotrimeric G protein α subunit Go**	**B**
(I) hmr-1	**Cadherin**	**B**
(I) kin-10	**Putative regulatory (β) subunit of casein kinase II**	**B**
(V) mom-2	**Member of the Wnt family**	**B**
(II) mpk-2	**Mitogen activated protein (MAP) kinase**	**B**
(I) pfd-3	**Putative prefoldin, orthologous to human VBP1**	**B**
(II) aakg-5	**AMP kinase**	**C**
(V) arx-2	**Subunit of the actin related protein of the conserved Arp2/3 complex**	**C**
(III) arx-3	**Subunit of the actin related protein of the conserved Arp2/3 complex**	**C**
(I) bub-1	**Serine/threonine kinase**	**C**
(V) chk-1	**CHK1-like serine threonin protein kinase**	**C**
(I) chp-1	**Protein containing two CHORD domains**	**C**
(I) csnk-1	**Ortholog of human CSNK1G3, CSNK1G1 and CSNK1G2**	**C**
(II) ect-2	**Putative RHO guanine nucleotide exchange factor (RhoGEF)**	**C**
(I) ekl-1	**Ortholog of members of the human TDRD**	**C**
(IV) fln-1	**Filamin**	**C**
(X) ifa-3	**Intermediate filament protein**	**C**
(III) klp-19	**Plus-end-directed microtubule motor protein**	**C**
(III) lit-1	**Serine threonine protein kinase**	**C**
(I) mei-2	**Novel protein containing a region similar to the p80-targeting subunit of katanin**	**C**
(V) mrck-1	**Serine/threonine-protein kinase**	**C**
(III) par-2	**Protein containing a C3HC4-type RING-finger**	**C**
(III) pfd-5	**Putative prefoldin 5 subunit**	**C**
(I) sys-1	**Novel protein that contains three divergent armadillo repeats**	**C**
(II) spv-1	**Ortholog of human GMIP**	**C**
(I) tbcd-1	**Putative β-tubulin folding cofactor D**	**C**
(I) usp-5	**Ortholog of human USP5 and USP13**	**C**
(II) Y19D2B.1	**Structural constituent of cytoskeleton**	**C**

*** Defect refers to lethality and body morphology defects**

Table S1

No enhanced defect* compared to wild-type

(I)	(II)	(III)	(IV)	(V)	(X)
afd-1	*aak-1*	*abce-1*	*arp-11*	*air-1*	*aakb-1*
arx-7	*arp-1*	*abi-1*	*ced-5*	*cct-7*	*aakg-2*
aspm-1	*C27H5.4*	*arf-1.2*	*dli-1*	*F14H3.12*	*abl-1*
chs-1	*cacn-1*	*cct-5*	*dnc-1*	*gck-2*	*dyn-1*
col-53	*cal-2*	*cct-6*	*dyci-1*	*knl-3*	*efn-3*
cpn-1	*ccm-3*	*cls-1*	*eps-8*	*mig-6*	*F20B6.1*
cutl-13	*cct-1*	*cls-2*	*frk-1*	*noca-1*	*frm-9*
dhc-1	*cct-2*	*col-94*	*gex-2*	*pak-2*	*hpk-1*
dlc-6	*cct-4*	*col-97*	*gex-3*	*par-1*	*ifa-2*
eak-6	*cdc-25.4*	*cra-1*	*klp-10*	*rbx-1*	*kin-29*
egg-5	*cpn-2*	*cyk-4*	*klp-11*	*spas-1*	*lam-2*
egg-6	*dep-1*	*daf-4*	*klp-5*	*sun-1*	*lin-18*
ekl-4	*ebp-2*	*fem-2*	*let-60*	*syx-5*	*lpr-3*
erm-1	*eff-1*	*frm-2*	*let-92*	*unc-112*	*nck-1*
fhod-1	*egg-3*	*gei-4*	*M116.5*	*unc-70*	*pak-1*
gei-17	*evl-20*	*gop-3*	*nsp-1*		*pfn-2*
gfi-2	*F59A6.5*	*ina-1*	*par-5*		*pfn-3*
gsa-1	*frm-5.2*	*inft-1*	*pfd-1*		*pqn-34*
gsk-3	*glb-12*	*kin-18*	*pld-1*		*unc-97*
gsp-3	*gpb-1*	*klp-6*	*pmk-2*		
gsp-4	*klp-1 / unc-104*	*klp-7*	*pmk-3*		
kca-1	*klp-17*	*let-805*	*ptp-4*		
lim-9	*let-268*	*mpk-1*	*rac-1 / ced-10*		
mel-26	*lrr-1*	*mtm-3*	*rack-1*		
mfap-1	*max-2*	*nfm-1*	*unc-33*		
mom-5	*mel-11*	*pef-1*	*wsp-1*		
nab-1	*mig-5*	*plk-1*	*zen-4*		
ned-8	*mlt-8*	*pph-6*			
nkb-1	*nsy-1*	*ptp-1*			
nmy-2	*pfd-2*	*pxl-1*			
npp-4	*pink-1*	*rfl-1*			
ocrl-1	*pir-1*	*tbb-2*			
pes-7	*ptc-3*	*ten-1*			
pfd-6	*ptp-2*	*tlk-1*			
ppk-1	*ptp-3*	*trd-1*			
rga-2	*saps-1*	*unc-116*			
rsa-1	*scpl-2*	*wrm-1*			
smgl-1	*sds-22*				
spd-1	*spdl-1*				
tba-2	*tac-1*				
ttx-7	*tba-4*				
unc-35	*unc-52*				
unc-59	*vab-19*				
unc-73	*vab-9*				
unc-73	*vhp-1*				
unc-94	*vps-11*				
vab-10	*vps-32*				
viln-1	*W0761.1*				
vps-20	*zyg-9*				
wve-1					

Global PBS /Predicted Biological Score/ *categories computed and established by Hybrigenics, to assess the interaction reliability*	
A	**Very high confidence in the interaction**
B	**High confidence in the interaction**
C	**Good confidence in the interaction**
D	**Moderate confidence in the interaction** */either due to false-positive interactions or due to interactions that are hardly detectable by the Y2H technique/*

Strongest candidates
/ Prey library: C. elegans embryo /

Primary Yeast Two Hybrid Screen */ Bait: CePAK-1 N-terminal amino acids: 1-294 /*		
Interactor candidate	***Protein function***	***Global PBS***
SPC-1	**α-spectrin**	**A**
F47B10.1	**ß-chain succinyl-co-A ligase**	**A**
CHW-1	**RhoU homolog**	**A**
GCK-1	**STE20-family kinase**	**A**
NCK-1	**NCK adaptor**	**A**
PIX-1 *	**ARHGEF7 homolog ß-Pix**	**A**
CDC-42 *	**Small GTPase**	**A**
PAK-1 *	**P21-activated Ser/Tre kinase (multiple hits through kinase domain)**	**A**
CED-10 *	**Rac-1 / Small GTPase**	**B**
POD-2	**Predicted acetyl-coA carboxylase**	**B**
Y39E4A.3	**Transketolase**	**B**
EEL-1	**HECT-ubiquitin ligase**	**C**
NPP-21	**Nuclear pore protein**	**C**
TAG-143	**Transcription factor**	**C**
UNC-44	**Ankyrin**	**D**
HIPR-1	**SLA2 and Hip related**	**D**
T05C1.4	**Conserved calmodulin-binding TFs**	**D**
Y53F4B.13	**RNA methyltransferase**	**D**
PTP-3	**LAR-like receptor tyr-protein phosphatase**	**D**
COGC-6	**Conserved Oligomeric Golgi (COG) Component**	**D**
DAF-21	**Hsp90 molecular chaperone family member**	**D**
GCK-1 variant	**STE20-family kinase**	**D**

Secondary Yeast Two Hybrid Screen */ Bait I: CeSPC-1 SR8-10(aa:796-1243) /* */ Bait II: CeSPC-1 SH3 (aa:986-1041) /* */ common hits using Bait I and Bait II /*		
Interactor candidate	***Protein function***	***Global PBS***
PAK-1	**p21-activated Kinase**	**A**
LIM-8	**LIM domain muscle component**	**A**
F44.E2.3	**ARGLU1 ortholog**	**A**
CSN-5	**COP9-subunit ortholog, E3 ubiquitin ligase interactor**	**A**
DEB-1	**Vinculin**	**A**
DnaJ	**DNAJ/ZRF1/MPP11 ortholog; ribosome-associated chaperone**	**B**
CYLD-1	**Human CYLD1 ortholog, NF-κβ signalling interactor**	**B**
VAB-3 / VAR-1	**Homeodomain protein PAX6 ortholog**	**B**
GRL-4	**Hedgehog-like protein**	**C**
UNC-34	**Enabled/VASP homolog**	**C**
T04F8.6	**Human ninein and ninein-like (GSK3B interactor) ortholog**	**D**
ALR-1	**Human ARX(aristaless) ortholog homeodomain transcription factor**	**D**
ATN-1	**α-actinin homolog**	**D**
MMCM-1	**Methylmalonyl-CoA mutase**	**D**
UNC-70	**β_G-spectrin**	**D**
VAB-10	**Spectraplakin**	**D**
F26A10.2	**Zinc-finger containing protein (required for germ line maintenance and locomotion)**	**D**
F43C1.1	**Human PHLPP1&PHLPP2 (PH domain&leucine-rich repeat Protein Phosphatase) ortholog**	**D**
ALP-1	**Enigma family member ALP (α-actinin associated LIM Protein) ortholog; required for actin anchorage**	**D**
CIT-1.2	**Cyclin T ortholog, embryonic transcriptional regulator**	**D**
FLH-1	**FLYWCH zinc finger transcription factor homolog**	**D**
SHW-1	**Human KCNC3 voltage-gated SHaW family potassium channel ortholog**	**D**

*** Positive controls (PAK-1 itself + its known interactors)**

Table S2

A	Shorter compared to *spc-1(-)*
B	Not shorter than *spc-1(-)*

Targeted gene	***Function***	***Strength of interaction***
(I) fhod-1	**Formin**	**A**
(I) hmr-1	**Cadherin**	**A**
(I) hmp-2	**β-catenin**	**A**
(II) cdc-42	**RHO GTPase**	**A**
(II) spdl-1	**Coiled-coil protein**	**A**
(II) vps-11	**Ortholog of human VPS11**	**A**
(III) mtm-3	**Myotubularin lipid phosphatase**	**A**
(III) mlc-5	**Myosin II essential light chain ortholog**	**A**
(IV) dnc-1	**Ortholog of the dynactin complex subunit p150/GLUED/DCTN1**	**A**
(IV) epi-1	**Laminin α chain**	**A**
(I) goa-1	**Ortholog of the heterotrimeric G protein α subunit Go**	**B**
(I) kin-10	**Putative regulatory (β) subunit of casein kinase II**	**B**
(I) mec-8	**mRNA processing factor**	**B**
(I) nmy-2	**Non-muscle myosin II**	**B**
(I) unc-94	**Tropomodulin**	**B**
(II) cap-2	**β subunit of actin capping protein**	**B**
(II) evl-20	**Ortholog of human ADP-ribosylation factor-like protein 2**	**B**
(II) spv-1	**Ortholog of human GMIP**	**B**
(II) unc-52	**Perlecan**	**B**
(III) klp-7	**Ortholog of human KIF2A, 2B and 2C**	**B**
(III) mup-4	**Transmembrane protein**	**B**
(IV) cap-1	**F-actin capping protein α subunit**	**B**
(IV) eps-8	**Cell signaling adaptor protein**	**B**
(IV) frk-1	**Non-receptor tyrosine kinase**	**B**
(IV) unc-33	**Conserved member of the CRMP/TOAD/Ulip/DRP family**	**B**

Table S3

Name	*Genotype*
DM3409	*mnDp33 (X;IV)/+ IV.; spc-1(ra409) X.*
DWP10	*fhod-1(tm2363) I.; qaIs8001 [unc-119(+) fhod-1::gfp]*
ML1694	*pix-1(gk416)X.*
ML1725	*mcEX567 [spc-1::GFP, myo-2p::mcherry]*
ML1822	*sma-1(ru18)V.; pak-1 (tm403)X.*
ML1943	*mcIs55[pak-1::GFP;pRF4]*
ML1911	*git-1(tm1962)X.*
ML2113	*mcIs67 [dpy7p::LifeAct::GFP; unc-119(+)] V.; stIs10088[hlh-1::his-24::mCherry, unc-119(+)]*
ML2129	*pak-1(tm403) X.*
ML2200	*pak-1(tm403) X.; mcIs67 [dpy7p::LifeAct::GFP; unc-119(+)] V; stIs10088[hlh-1::his-24::mCherry, unc-119(+)]*
ML2419	*mcEx915[ppak-1::pak-1::mkate;pR4(rol);pBSK]*
ML2428	*sma-1(ru18)V.*
ML2436	*spc-1(ra409) X.; mcEx636 [spc-1p::spc-1::GFP]*
ML2446	*pak-1(tm403) X.; spc-1(ra409) X.; mcEx636 [spc-1p::spc-1::GFP]*
ML2465	*mcIs91[linc26p::ABD::mkate; myo-2p::mcherry]*
ML2684	*mcEx1008 [fhod-1 ΔFH2/DAD]*
ML2688	*pak-1(tm403) X.; mcEx1009 [fhod-1 ΔFH2/DAD]*
ML2853	*pak-1(tm403) X.; mcEx1002 [fhod-1 ΔFH1/FH2/DAD]*
ML2854	*pak-1(tm403) X.; mcEx1003 [fhod-1 ΔDAD]*
ML2855	*pak-1(tm403) X.; mcEx1004 [fhod-1 full length]*
ML2856	*mcEx1005 [fhod-1 ΔFH1/FH2/DAD]*
ML2857	*mcEx1006 [fhod-1 ΔDAD]*
ML2858	*mcEx1007 [fhod-1 full length]*
N2	*Bristol*
XA8001	*fhod-1(tm2363) I.*

Table S4